

# Chapter 3

## Weakly nonlinear models

### 3.1 Introduction

In this chapter we will move beyond simple linear models and start to cover weakly nonlinear effects. We will use ideas from bifurcation theory and pattern formation to construct fairly general models, which will allow us to learn something about how convective patterns change as the inclination of the field is varied. In the next chapter, we will also use this work as a starting point for building more detailed models.

Consider first of all the case of a vertical magnetic field. In the previous chapter, we investigated the linear stability of the trivial solution, finding that for large enough Rayleigh number, the layer became unstable to roll-like (plane wave) perturbations of the form  $\exp i\mathbf{k} \cdot \mathbf{x}$ . At the critical Rayleigh number, we found that there was a circle of critical modes, with  $|\mathbf{k}| = k_c$ , which were neutrally stable; all other modes decayed exponentially. For  $R$  slightly above critical, there was a narrow annulus of modes in Fourier space, with wavenumbers close to  $k_c$ , which could grow exponentially.

We can use this linear analysis to try to predict what we might see when  $R$  is just above critical. We might expect the convection to take the form of rolls, with wavenumber  $|\mathbf{k}|$  equal to (or very close to)  $k_c$ . However, there are an infinite number of such modes, because of the rotational symmetry of the problem; any wavevector lying on the critical circle  $|\mathbf{k}| = k_c$  will do. Moreover, we can superpose two or more of these roll modes to obtain a new pattern. Examples of this are shown in Figure 3.1, which shows how hexagons can be obtained by superposing three sets of rolls at  $120^\circ$  to each other, and how squares can be produced by superposing two sets of rolls at right angles.

Linear theory alone cannot distinguish between a single roll mode, or a superposi-

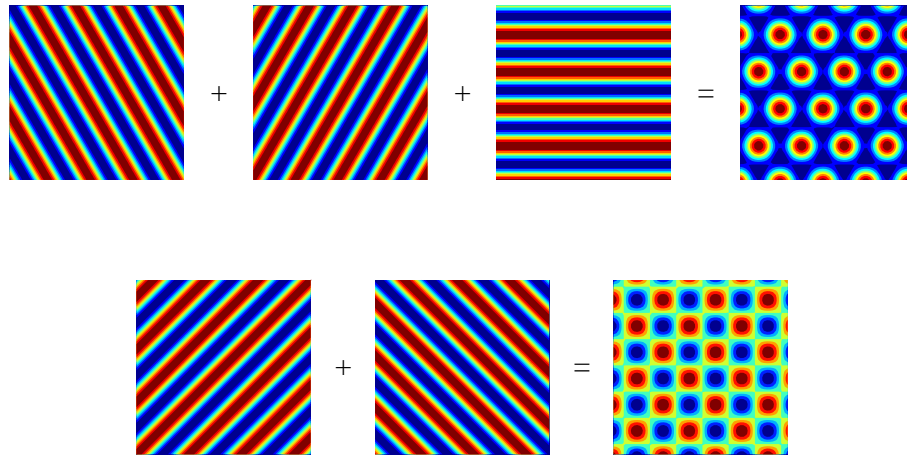


**Figure 3.1:** Hexagon and square patterns. The first line shows a hexagonal pattern, created by adding together three sets of rolls at an angle of  $120^\circ$  to each other. The second line shows a square pattern, created by superposing two sets of rolls at right angles to each other.

tion such as those shown in Figure 3.1, because the different modes would all evolve completely independently of each other. However, once we add nonlinearities into the problem, interactions between the different Fourier modes become possible. This means that the theory can now distinguish between the different patterns, and we will be able to predict which of the patterns we would see near onset. If the nonlinearities are assumed to be weak, it is possible to model the nonlinear interactions based on minimal assumptions about the underlying physics, which is what we will do in the rest of this chapter.

## 3.2 General notes on pattern formation

In this section we will explain some general methods that are used for studying pattern formation in weakly nonlinear systems. (In the following sections, we will go on to show how these methods can be applied in particular cases.)

A standard method of dealing with systems close to a bifurcation point (in our case, with  $R$  only just above  $R_c$ ) is to apply the centre manifold theorem. This allows us to simplify the problem by considering only the dynamics on the (extended) centre manifold. Basically, this can be thought of as eliminating all modes of wavenumber not equal to  $k_c$ ; these are ‘fast’ modes which decay exponentially with time. The critical modes, with wavenumber equal to  $k_c$ , constitute the slow dynamics. Unfortunately, with

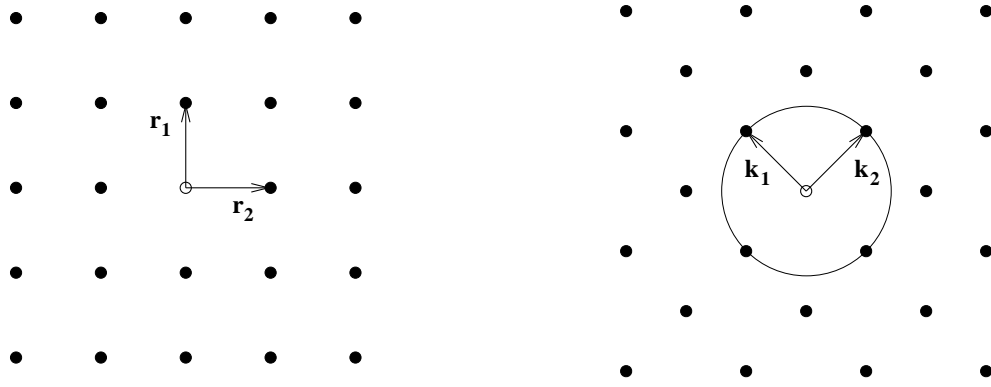


**Figure 3.2:** A periodic square lattice. The left-hand picture shows the lattice in real space, and the right-hand picture shows the ‘dual’ lattice in Fourier space.

the problem in its present form, the conditions of the centre manifold theorem are not met, for two reasons: firstly, there are an infinite number of critical modes, occupying the circle  $|\mathbf{k}| = k_c$ ; secondly, the non-critical modes can be arbitrarily close to this circle and have growth rates which can be arbitrarily close to zero.

One way to avoid both of these problems is to restrict ourselves to solutions which are doubly periodic on some lattice; in other words, if we denote the solution by  $\Psi(\mathbf{x})$ , then there should exist two ‘lattice vectors’,  $\mathbf{r}_1$  and  $\mathbf{r}_2$ , such that for all integers  $n_1$  and  $n_2$  and for all  $\mathbf{x}$ ,  $\Psi$  satisfies  $\Psi(\mathbf{x} + n_1\mathbf{r}_1 + n_2\mathbf{r}_2) = \Psi(\mathbf{x})$ .

This restriction to a doubly periodic lattice can also be thought of as a restriction on the Fourier transform of the solution. If we consider possible Fourier modes  $\exp i\mathbf{k} \cdot \mathbf{x}$ , then clearly only certain wavevectors  $\mathbf{k}$  will produce a function which is doubly periodic on the given lattice. The set of such wavevectors  $\mathbf{k}$  itself forms a lattice, in Fourier space, which is known as the *dual lattice*.

These concepts are best explained by giving examples. Two lattices which are commonly used in these sorts of problems are the square and hexagonal lattices (so-called because they admit the square and the hexagonal patterns from Figure 3.1).

The square lattice is illustrated in Figure 3.2. The left-hand picture shows the two lattice vectors  $\mathbf{r}_1$  and  $\mathbf{r}_2$ , together with the lattice points themselves (i.e. points of the form  $n_1\mathbf{r}_1 + n_2\mathbf{r}_2$  for  $n_1$  and  $n_2$  integer). For the square pattern, these points would correspond to the centres of the squares. The right-hand picture shows the dual lattice vectors  $\mathbf{k}_1$  and  $\mathbf{k}_2$ , together with the dual lattice points (points of the form  $n_1\mathbf{k}_1 + n_2\mathbf{k}_2$  for  $n_1$  and  $n_2$  integer). The points of the dual lattice do not correspond to physical

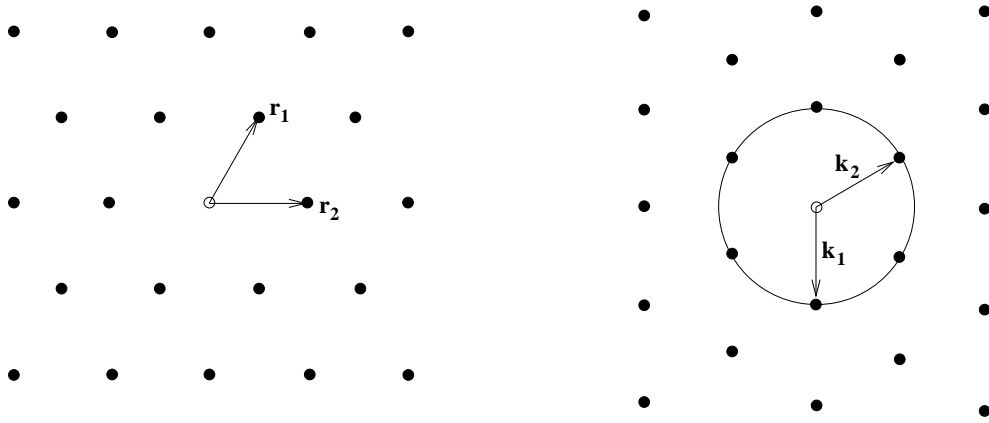


**Figure 3.3:** *The equivalent of Figure 3.2 for the hexagonal lattice.*

points but rather to wavevectors of ‘admissible’ Fourier modes. The equivalent diagram for the hexagonal lattice is shown in Figure 3.3. (The other common type of lattice is the ‘rhombic’ lattice, where the angle between the two wavevectors  $\mathbf{k}_1$  and  $\mathbf{k}_2$  takes a general value, equal to neither  $90^\circ$  nor  $120^\circ$ .)

If we scale our lattice such that the dual vectors  $\mathbf{k}_1$  and  $\mathbf{k}_2$  are of length  $k_c$ , then the critical circle will intersect four wavevectors (in the square or rhombic case) or six wavevectors (in the hexagonal case), as illustrated in the diagram. In other words, whilst in the full problem there was an entire circle of critical modes, once we restrict to a periodic lattice, there are a finite number of permissible critical modes. Moreover, all other modes on the dual lattice are a finite distance away from the critical circle  $|\mathbf{k}| = k_c$ , and therefore their growth rates are bounded away from zero. Hence, both of the difficulties mentioned above are resolved, and we can reduce the problem to the evolution of a small number of modes on the extended centre manifold.

Thus, the restriction to a periodic lattice greatly simplifies the mathematics, but it also unfortunately restricts the set of possible patterns that can be investigated. For example, if we chose the square lattice, we could look at rolls and square patterns. The hexagonal lattice allows rolls and hexagons as well as some other patterns (e.g. triangles and rectangles), but it leaves out the squares. (There is no lattice on which both squares and hexagons can exist simultaneously.) The results must be interpreted with this in mind, although usually we have some physical intuition about the problem, which can inform the decision of which lattice is most appropriate to a particular situation.

Therefore we are led to consider a superposition of  $N$  different roll modes. In the

case of a steady bifurcation, the solutions will take the following form:

$$\Psi = \sum_{j=1}^N z_j(t) e^{i\mathbf{k}_j \cdot \mathbf{x}} \Psi_0^{(j)} + \text{c.c.} \quad (3.1)$$

Here  $\Psi$  stands for (one or more of) the physical variables from the original problem ( $\mathbf{u}$ ,  $\mathbf{B}$  etc.). The  $\mathbf{k}_j$  are the wavevectors of each mode intersecting the critical circle  $|\mathbf{k}| = k_c$ . Any vertical dependence has been factored out into  $\Psi_0^{(j)}$  (which essentially represents the vertical eigenfunction of the mode). The  $z_j$  are complex functions of time representing the amplitudes of the different modes.

In the case of the square lattice, it appears that  $N = 4$ , since four points on the dual lattice intersect the critical circle; see Figure 3.2. However, in fact  $N$  is only 2; this is because wavevectors  $\mathbf{k}$  and  $-\mathbf{k}$  are in fact equivalent (the *direction* of the wavevector determines the orientation of a mode, but its *sense*, either  $+$  or  $-$ , is irrelevant). Similarly, for steady bifurcation on a hexagonal lattice,  $N = 3$  and not 6.

For an oscillatory bifurcation, the form is slightly different:

$$\Psi = \sum_{j=1}^N (z_j(t) e^{i\mathbf{k}_j \cdot \mathbf{x}} + w_j(t) e^{-i\mathbf{k}_j \cdot \mathbf{x}}) e^{-i\omega t} \Psi_0^{(j)} + \text{c.c.} \quad (3.2)$$

Note the addition of the  $\exp(-i\omega t)$  term, which represents the oscillation frequency of each mode. This time there *is* a difference between wavevectors  $\mathbf{k}$  and  $-\mathbf{k}$ ; the sense of the wavevector indicates the direction of travel of each mode (each mode can travel in one of two directions).

Our objective now is to come up with a set of ordinary differential equations that govern the time evolution of the  $z_j$ . These are known as the *amplitude equations*. In linear theory they would be very simple:  $\dot{z}_j = s z_j$ , where  $s$  is the corresponding linear growth rate. In weakly nonlinear theory we have to add further terms representing nonlinear interactions between the different modes. These would generally be determined from a perturbation analysis of the original partial differential equations; the required amplitude equations usually come out as a solvability condition.

However, we do not need to go to such lengths to gain some useful insight into the problem. Rather, we can make use of symmetry. We know that the problem possesses certain symmetries; in our case, the relevant symmetries are rotations, reflections and translations of the plane, which together form the Euclidean symmetry group  $E(2)$ . (More specifically, we must consider the subset of  $E(2)$  that leaves our periodic lattice invariant.) The amplitude equations must be consistent with these symmetries; not just

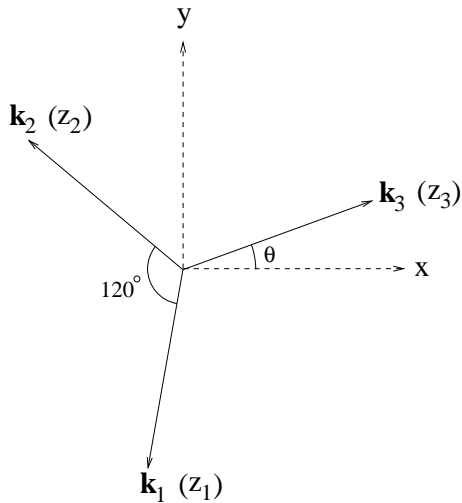


**Figure 3.4:** Diagram showing the three wavevectors  $\mathbf{k}_j$  and their corresponding amplitudes  $z_j$  ( $j = 1, 2, 3$ ), for the steady hexagonal model. Note the orientation (represented by the angle  $\theta$ ); the direction of tilt of the magnetic field is along the  $x$ -axis.

any amplitude equations are allowed. Together with the assumption that the amplitudes are small, this usually provides enough information to constrain the amplitude equations quite strongly; typically the form of the equations is known, but there are one or more undetermined coefficients.

We will now consider how these principles apply to particular choices of periodic lattice.

### 3.3 Steady bifurcation on a hexagonal lattice

We start with the hexagonal lattice, since this is a natural choice for magnetoconvection, for the following reason. From studies of magnetoconvection in vertical fields, we expect to see a pattern of hexagons near onset. When the field is tilted we would presumably still see a (slightly distorted) hexagonal pattern, but when the field is nearly horizontal, the preferred pattern will be field-aligned rolls (Danielson, 1961). The interesting question is what happens for field inclinations in between these two extremes.

To investigate this competition between hexagons and rolls, we consider the hexagonal lattice, with three wavevectors  $\mathbf{k}_1$ ,  $\mathbf{k}_2$  and  $\mathbf{k}_3$ , as illustrated in Figure 3.4. The angle  $\theta$  represents the orientation of the lattice; this is unimportant when the field is vertical (because of the rotational symmetry), although it will become important later on, when

we introduce non-vertical fields.

Staying with a vertical magnetic field for the moment, we can determine the most general amplitude equations satisfying the symmetry requirements. (The relevant symmetry group is the subset of  $E(2)$  that leaves the hexagonal lattice invariant, which is the group  $T^2 \rtimes D_6$ ;  $T^2$  represents  $x$  and  $y$  translations, while  $D_6$  represents rotational and reflectional symmetries of the hexagonal lattice.) This is actually a well-known, standard problem (e.g. Golubitsky et al. 1984). The equations are:

$$\dot{z}_1 = \mu z_1 + \alpha \bar{z}_2 \bar{z}_3 - \gamma z_1 (|z_1|^2 + \beta |z_2|^2 + \beta |z_3|^2) \quad (3.3)$$

$$\dot{z}_2 = \mu z_2 + \alpha \bar{z}_3 \bar{z}_1 - \gamma z_2 (|z_2|^2 + \beta |z_3|^2 + \beta |z_1|^2) \quad (3.4)$$

$$\dot{z}_3 = \mu z_3 + \alpha \bar{z}_1 \bar{z}_2 - \gamma z_3 (|z_3|^2 + \beta |z_1|^2 + \beta |z_2|^2) \quad (3.5)$$

The coefficients  $\alpha$ ,  $\beta$ ,  $\gamma$  and  $\mu$  are all real. These will depend on the various parameters in the original problem ( $Q$ ,  $\zeta$ , etc.) and we cannot determine their values without more detailed calculations. Clearly, however, we can see that  $\mu$  will be an increasing function of  $R$ , with  $\mu = 0$  when  $R = R_c$ . The coefficient  $\alpha$  represents the amount of up-down symmetry breaking; it is zero in an up-down symmetric case (such as Boussinesq convection).

We have dropped terms higher than third order, which may be justified by assuming the following scalings. The small parameter in the problem is the amount by which the Rayleigh number exceeds critical (i.e.,  $R - R_c$ ). If we define  $\epsilon$  such that  $R - R_c \propto \epsilon^2$ , then the amplitudes  $|z_j|$  are of order  $\epsilon$ . We must also assume for consistency that  $\alpha = O(\epsilon)$ , i.e. that the amount of up-down symmetry breaking is small. Each term is then of the same order ( $\epsilon^3$ ), and all the neglected terms are of higher order.

By rescaling time and the amplitudes, we can assume without loss of generality that  $\alpha = \gamma = 1$ . We cannot scale out  $\beta$ , but we do make the assumption that  $\beta > 1$ , which ensures that rolls are stable in the absence of the quadratic term (which is the case for convection).

We may also take the  $z_j$  to be real (after a shift of origin if necessary). This can be shown quite easily by writing out the equations in terms of amplitudes and phases of the  $z_j$ ; see e.g. Malomed et al. (1994).

We now turn to solutions of these equations. The bifurcation diagram as  $\mu$  is varied is shown in Figure 3.5. The trivial solution,  $z_1 = z_2 = z_3 = 0$ , is stable for  $\mu$  negative and unstable for  $\mu$  positive. There is a branch of rolls (e.g.  $z_1 = \sqrt{\mu}$ ,  $z_2 = z_3 = 0$ ), which bifurcates supercritically from  $\mu = 0$ , and is stable for  $\mu$  sufficiently large. The

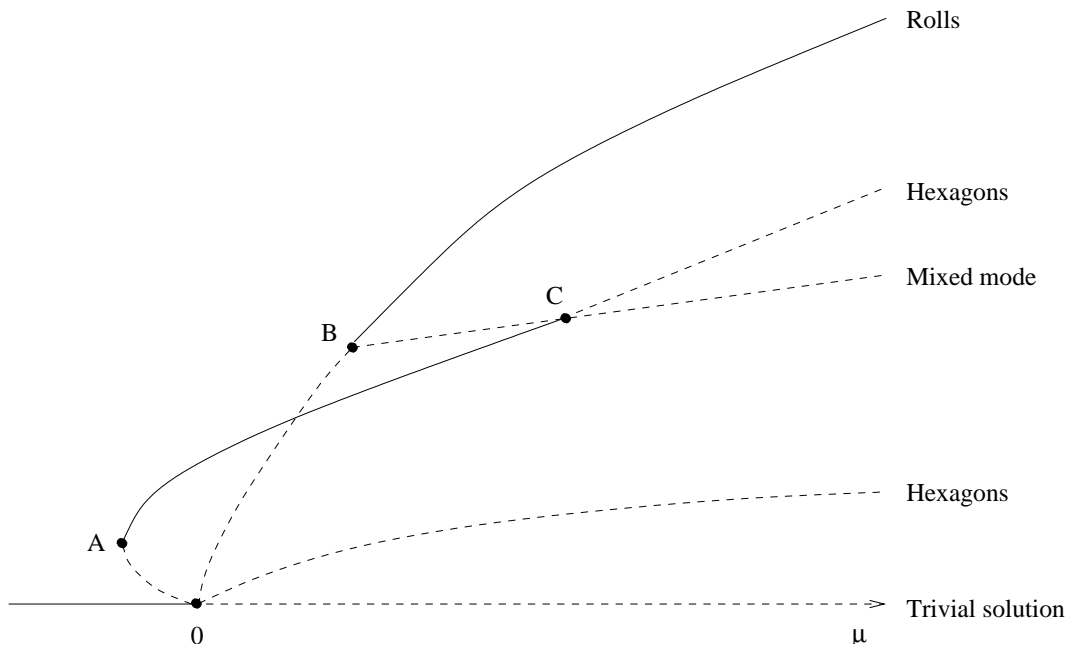


**Figure 3.5:** Bifurcation diagram for the symmetric case (when all three linear growth rates are equal). The bifurcations A, B and C occur at the following values of  $\mu$ : A at  $\mu = -1/(4 + 8\beta)$ ; B at  $\mu = 1/(\beta - 1)^2$ ; C at  $\mu = (\beta + 2)/(\beta - 1)^2$ .

bifurcation at which the rolls gain stability also creates a branch of mixed modes, which are rectangular in appearance, and have (e.g.)  $z_1 = z_2 \neq z_3$ ; this solution is always unstable.

Finally, there are also two branches of hexagons. These are related by a sign change (in the three  $z_j$ ). The uppermost branch can be stable (for some  $\mu$  values at least) while the lower branch is always unstable (and hence unobservable). In convection, one branch would represent a solution with upflows at the centre of each convection cell (so-called ‘up’ hexagons), while the other would have downflows there (‘down’ hexagons). In general, we cannot say which is which, i.e. we cannot say whether the uppermost, stable branch corresponds to the ‘up’ or to the ‘down’ hexagons. For compressible convection, however, we know that the ‘up’ hexagons are the stable solution (as is confirmed by numerical simulations, for example; see also section 1.5.1).

The problem also contains hysteresis. This occurs in two separate ranges of  $\mu$  values. The first is between points A and O on Figure 3.5, where hexagons and the trivial solution are simultaneously stable. This indicates that the onset of convection itself is associated with hysteresis. The second region of hysteresis occurs between points B and C, where there is bistability between rolls and hexagons. This indicates that the

transition between hexagons (for smaller  $\mu$ ) and rolls (for larger  $\mu$ ) is hysteretic.

### 3.3.1 Weakly breaking the isotropy

So far, we have considered only vertical fields. When the field is tilted, anisotropy is introduced and the symmetry between the three different modes is broken. The translational symmetry remains, as does the reflection symmetry  $y \rightarrow -y$ , but the other reflection symmetries, as well as the isotropy, are lost. We could repeat the analysis using the new (smaller) symmetry group, and come up with a different set of ordinary differential equations for the  $z_j$ . However, it is more enlightening to consider a situation where the symmetry is only *weakly broken*. For example, if we consider a small tilt angle  $\phi$ , then the problem is strictly speaking anisotropic, but we are still very close to the isotropic situation, and this can be exploited.

We will model this by breaking the symmetry in the linear terms only, replacing the single value  $\mu$  with different values  $\mu_1$ ,  $\mu_2$  and  $\mu_3$  in each equation. Strictly speaking the other coefficients ( $\alpha$ ,  $\beta$  and  $\gamma$ ) should be changed as well, but this is not actually necessary to break the symmetry, and we will just leave them unchanged. (We will justify this further below.)

The new equations, with weakly broken symmetry, are:

$$\dot{z}_1 = \mu_1 z_1 + \alpha \bar{z}_2 \bar{z}_3 - \gamma z_1 (|z_1|^2 + \beta |z_2|^2 + \beta |z_3|^2) \quad (3.6)$$

$$\dot{z}_2 = \mu_2 z_2 + \alpha \bar{z}_3 \bar{z}_1 - \gamma z_2 (|z_2|^2 + \beta |z_3|^2 + \beta |z_1|^2) \quad (3.7)$$

$$\dot{z}_3 = \mu_3 z_3 + \alpha \bar{z}_1 \bar{z}_2 - \gamma z_3 (|z_3|^2 + \beta |z_1|^2 + \beta |z_2|^2) \quad (3.8)$$

Since we now have two small quantities, the tilt angle  $\phi$  and the ‘effective’ Rayleigh number  $r \equiv (R - R_c)/R_c$ , it is important to clarify the scalings involved. We introduce a small parameter  $\epsilon$  and scale  $\phi$  as  $O(\epsilon)$ , while  $r$  is (as before) taken to be  $O(\epsilon^2)$ . We can now write the  $\mu_j$  as functions of both  $r$  and  $\phi$ . The correct form for small  $\epsilon$  is

$$\mu_j = A_j \phi^2 + B_j i \phi + Cr + O(\epsilon^3), \quad (3.9)$$

where  $A_j$ ,  $B_j$  and  $C$  are real constants, with  $A_1 \geq A_2 \geq A_3$ . (The argument that the growth rates must take this form for small  $\phi$  was given in the previous chapter.) Ignoring the imaginary parts (for the moment), each  $\mu_j$  is of order  $\epsilon^2$ , and the amplitudes  $|z_j|$  may be scaled to be  $O(\epsilon)$ . We also assume once again that  $\alpha = O(\epsilon)$ ; each term on the right-hand side is then of the same order ( $\epsilon^3$ ).

Unfortunately, the imaginary parts of the  $\mu_j$  appear at order  $\epsilon$  and thus do not satisfy this balance. However, we can deal with this by making a Galilean transformation. To show this we first of all write  $z_j = R_j e^{i\psi_j}$  (with  $R_j$  and  $\psi_j$  real) and decompose (3.6)–(3.8) into amplitude and phase equations:

$$\dot{R}_1 = \mu_{1r} R_1 + \alpha R_2 R_3 \cos \Psi - \gamma(R_1^2 + \beta R_2^2 + \beta R_3^2) R_1 \quad (3.10)$$

$$\dot{R}_2 = \mu_{2r} R_2 + \alpha R_3 R_1 \cos \Psi - \gamma(R_2^2 + \beta R_3^2 + \beta R_1^2) R_2 \quad (3.11)$$

$$\dot{R}_3 = \mu_{3r} R_3 + \alpha R_1 R_2 \cos \Psi - \gamma(R_3^2 + \beta R_1^2 + \beta R_2^2) R_3 \quad (3.12)$$

$$\dot{\Psi} = \Omega - \alpha \left( \frac{R_2 R_3}{R_1} + \frac{R_3 R_1}{R_2} + \frac{R_1 R_2}{R_3} \right) \sin \Psi. \quad (3.13)$$

Here  $\Psi = \psi_1 + \psi_2 + \psi_3$  and  $\Omega = \mu_{1i} + \mu_{2i} + \mu_{3i}$ . (Note that the ‘r’ and ‘i’ subscripts refer to real and imaginary parts; e.g.  $\mu_1 = \mu_{1r} + i\mu_{1i}$ .)

When  $\phi = 0$ ,  $\Omega = 0$  and (3.13) shows that  $\Psi$  tends to zero. This means that we can take all three  $z_j$  to be real. To see this, note that we have two translational degrees of freedom, so we can set two of the  $\psi_j$  to zero by shifting the origin. The condition  $\Psi = 0$  then implies that all three  $\psi_j$  are zero, i.e. all  $z_j$  are real.

When  $\phi \neq 0$  it appears that  $\Omega$  will become non-zero (see equation 3.9), invalidating the argument. However in our problem it can be shown that  $B_1 + B_2 + B_3 = 0$  (see below), so that  $\Omega$  is in fact  $O(\epsilon^3)$ ; to balance (3.13),  $\Psi$  must then remain of order  $\epsilon$ . Therefore in (3.10)–(3.12), we should consistently set  $\cos \Psi = 1$  at this order;  $\Psi$  then decouples and the net result is that we are left with (3.6)–(3.8) again, except that now the imaginary parts of the  $\mu_j$  can be ignored and one can assume that all the  $z_j$  (and  $\mu_j$ ) are real. (Therefore, we will drop the suffix ‘r’ from now on, writing  $\mu_j$  in place of  $\mu_{jr}$ .) This is equivalent to transforming to a moving frame in which the patterns appear steady.

The condition  $B_1 + B_2 + B_3 = 0$  is in fact clear from a small- $\phi$  expansion (up to first order) of the linearized equations of the previous chapter (equations 2.15–2.23). Since  $\phi$  now appears only in the combination  $k_x \phi$ , it can be seen that the equations are now invariant under rotations of the wavevector  $\mathbf{k}$  as long as one adjusts  $\phi$  to ensure that  $k_x \phi$  remains unchanged. Therefore, since we know that the oscillation frequency is proportional to  $\phi$  at this order, this argument shows that it is also proportional to  $k_x$  (at fixed  $|\mathbf{k}|$ ). Hence, since  $k_{1x} + k_{2x} + k_{3x} = 0$ , it follows that  $B_1 + B_2 + B_3 = 0$ .

We can now explain why we do not have to break the symmetry in the coefficients  $\alpha$ ,  $\beta$  and  $\gamma$ , i.e. why we do not have to write out separate values  $\alpha_1$ ,  $\alpha_2$  and  $\alpha_3$  in the three equations rather than just the single value  $\alpha$  (and similarly for  $\beta$  and  $\gamma$ ). Clearly, all

three  $\alpha_j$  must be equal when  $\phi = 0$ , and so we have  $\alpha_j = \alpha + O(\phi)$ ; since  $\phi = O(\epsilon)$ , the corrections that this would produce would all appear at fourth order in  $\epsilon$  (at least). Since we are dropping all terms of order  $\epsilon^4$  and higher, these corrections should be consistently neglected, and the symmetry should be maintained in  $\alpha$ ; the same applies to  $\beta$  and  $\gamma$ . (Another way of putting this is that there exists a near-identity transformation that reduces the system to the above form.) Conversely, note that with these scalings the asymmetry in  $\mu$  appears at order  $\epsilon^3$ , and the broken symmetry in  $\mu$  must be included.

As before, we assume  $\beta > 1$ , and rescale time and the amplitudes to ensure that  $\alpha = \gamma = 1$ . By rescaling  $\phi$  and  $r$ , we can also choose  $A_3 = 1$  and  $C = 1$ .

We remark that once the isotropy is broken (for  $\phi \neq 0$ ), the orientation of the hexagonal lattice, represented by the angle  $\theta$  on Figure 3.4, is now important. Note that without loss of generality we can choose  $0^\circ \leq \theta \leq 30^\circ$ . This is for two reasons: firstly, the lattice itself is invariant under rotations by  $60^\circ$  (with a corresponding cyclic permutation of the  $\mathbf{k}_j$  and  $z_j$ ); secondly, the  $y \rightarrow -y$  reflection symmetry means that  $\theta$  and  $-\theta$  will be equivalent, which halves the range of angles that must be considered.

The angle  $\theta = 30^\circ$  would probably be the most relevant choice, since the linear theory showed that parallel rolls (with the wavevector pointing in the  $y$ -direction) were the most unstable mode, and this mode is included (as  $\mathbf{k}_1$ ) when  $\theta = 30^\circ$ . However, it is interesting to look at other values of  $\theta$  as well, because in a sense, all modes would be present in the full problem (for example, if numerical simulations were to be performed).

This problem, in the form (3.10)–(3.12), has been studied before, although in a different context, by previous authors. Malomed et al. (1994) give bifurcation diagrams which use  $(\mu_1, \mu_2, \mu_3)$  directly as bifurcation parameters; these are not directly related to our parameters  $r$  and  $\phi$ . Nevertheless they provide several useful analytic results which we have made use of in this chapter. Matthews (1998) has produced bifurcation diagrams showing how the standard picture of Figure 3.5 changes once the symmetry is broken – we have reproduced these below, since they are directly equivalent to our problem in the case when  $\phi$  is held fixed at a small non-zero value, and  $r$  is changed.

### 3.3.2 Changes to the bifurcation diagrams

Once the symmetry is broken, the bifurcation diagrams of Figure 3.5 undergo several changes. The first relates to the roll solutions. Previously, the three possible orientations of rolls all had the same properties, because they were related by symmetry; therefore

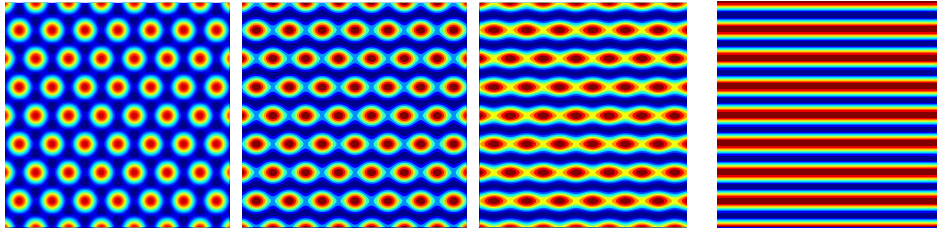


**Figure 3.6:** Distortion from a pure hexagon solution as the asymmetry is increased.

there was effectively only one branch of rolls. Now that the symmetry is broken, this splits into three separate branches, one for each possible orientation, and each having slightly different properties. We will denote the roll branch with  $z_j$  non-zero by  $R_j$ . The solution  $R_1$  is stable if

$$2\beta\mu_1 - \mu_2 - \mu_3 > 0 \quad \text{and} \quad (\beta\mu_1 - \mu_2)(\beta\mu_1 - \mu_3) > \mu_1 \quad (3.14)$$

(Malomed et al., 1994).

The second change relates to the hexagon and rectangle (or mixed mode) branches. Previously we could make a clear distinction between the hexagons and the rectangles, in the sense that hexagons have  $z_1 = z_2 = z_3$ , while rectangles have e.g.  $z_1 = z_2 \neq z_3$ . Once the symmetry is broken, this distinction does not apply, and we can only really describe these branches as ‘mixed modes with all three  $z_j$  different’. However, since the symmetry breaking is weak, we will still be able to recognize the mixed mode branches as slightly distorted versions of the original patterns (either hexagons or rectangles). Therefore, we will continue using the name ‘hexagons’ (and the label  $H$ ) for the stable ‘mixed mode’ branch, although it should be understood that these are not perfectly regular hexagons, but are instead slightly distorted in appearance.

This effect is illustrated in Figure 3.6, where we have plotted a pure hexagon solution ( $|z_1| = |z_2| = |z_3|$ ) at the far left, a pure roll solution ( $z_2 = z_3 = 0$ ) at the far right, and ‘distorted hexagon’ solutions (with  $|z_1| > |z_2| = |z_3|$ ) in between. For very weakly broken symmetry (second picture), the solutions are only slightly distorted from the original hexagon pattern, but for more strongly broken symmetry (third picture) the pattern becomes much closer to the rolls in appearance.

We will now plot bifurcation diagrams showing how Figure 3.5 changes once the symmetry is broken. We do this in three different cases. The first (corresponding to the work of Matthews 1998) has  $\phi$  fixed and  $r$  varying. The second is the reverse, with fixed  $r$  and variable  $\phi$ . Finally, we plot diagrams for the general case where both  $r$  and  $\phi$

Solution	Condition for stability	$\phi_{\text{pf}}^2$
$R_1$	(always)	$\frac{A_1}{(\beta A_1 - A_2)(\beta A_1 - 1)}$
$R_2$	$A_1 < \min(2\beta A_2 - 1, \beta A_2)$	$\frac{A_2}{(\beta A_2 - A_1)(\beta A_2 - 1)}$
$R_3$	$\beta > \max(A_1, A_2)$	$\frac{1}{(\beta - A_1)(\beta - A_2)}$

**Table 3.1:** Stability properties for rolls. There are two possibilities. If the condition in the second column is met then the rolls are stable for  $\phi^2 > \phi_{\text{pf}}^2$  where  $\phi_{\text{pf}}^2$  is given in the third column. If the condition in the second column is not met then the rolls are never stable.

are allowed to vary, although for simplicity we have restricted this to the special values  $\theta = 0^\circ$  and  $\theta = 30^\circ$ .

### Bifurcation diagrams for fixed $\phi$

The bifurcation diagrams given by Matthews (1998), reprinted in Figure 3.7, correspond to taking a fixed small value of  $\phi$  and allowing  $r$  to vary.<sup>1</sup> Apart from the roll branch splitting into two or three separate branches, as mentioned above, the changes from the isotropic case are minimal: both regions of hysteresis still exist, and we still have the stable trivial solution for low  $r$  and stable hexagons for intermediate  $r$ . There is one other change, relating to the rolls: they are stable for large  $r$  as before, but they can also be stable in a (very narrow) range of  $r$  values near the initial bifurcation from the trivial solution. (This occurs for  $\theta \neq 0^\circ$ .)

### Bifurcation diagrams for fixed $r$

We consider the case  $r = 0$ , which corresponds to setting the Rayleigh number equal to the critical Rayleigh number for a vertical field (so that the trivial solution is neutrally stable when  $\phi = 0$ ). We then allow the tilt angle to increase above zero. As this is done, the critical Rayleigh number falls (because of the decreasing vertical component of the magnetic field, as was discussed in the previous chapter), and so the growth rates for the three modes become positive. (In other words, there should be a bifurcation at  $\phi = 0$  at which the three roll modes appear.)

<sup>1</sup>These figures are from Matthews (1998), ©1998 Elsevier, reproduced with permission.

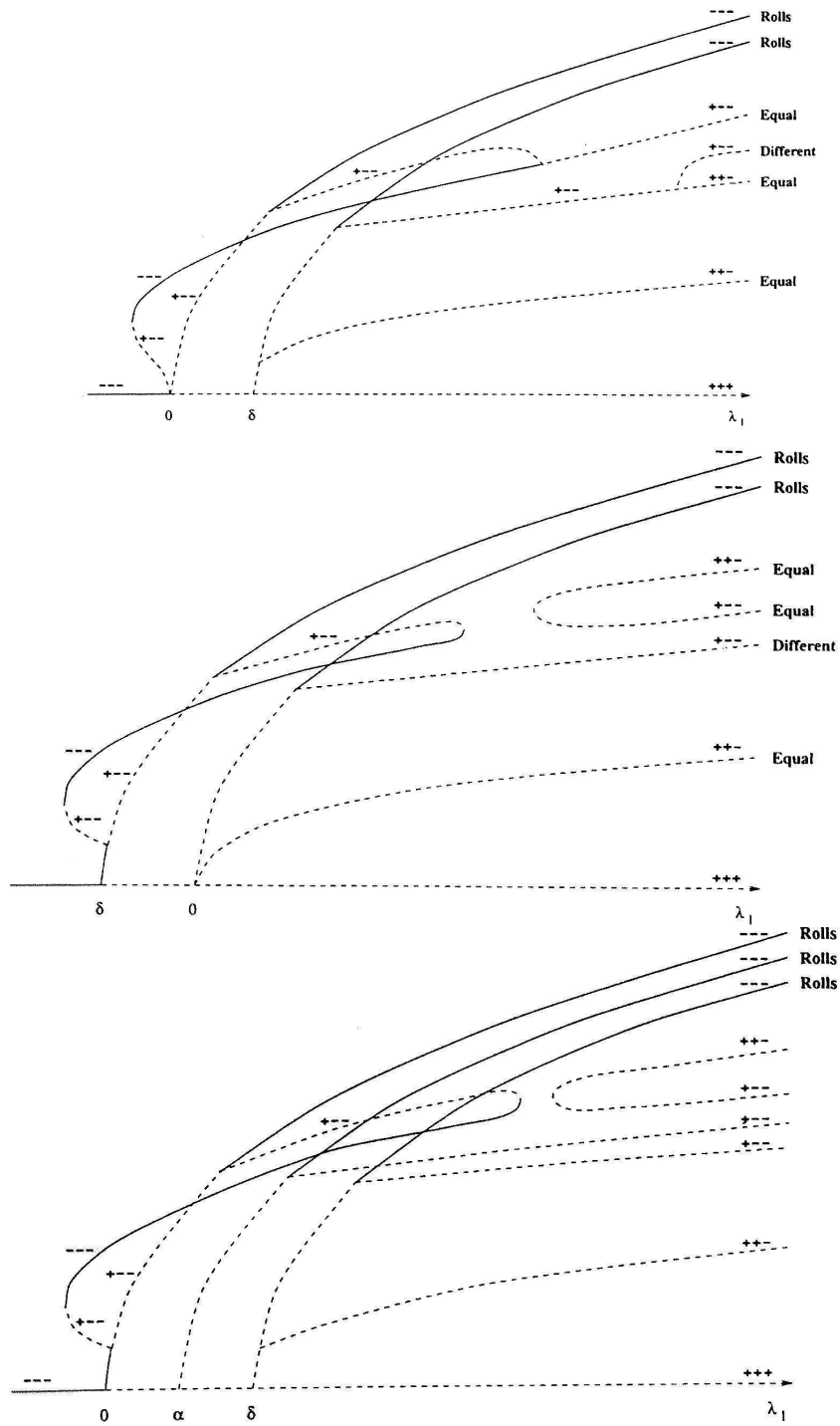


**Figure 3.7:** Bifurcation diagrams (from Matthews 1998) showing the changes to Figure 3.5 once the symmetry is broken. Note that Matthews'  $\lambda_1$  corresponds to our  $r$  (with  $\phi$  fixed at a small non-zero value). The three pictures correspond to different values of  $\theta$ , as follows: Top picture:  $\theta = 0^\circ$ ; middle picture:  $\theta = 30^\circ$ ; bottom picture:  $0^\circ < \theta < 30^\circ$ .

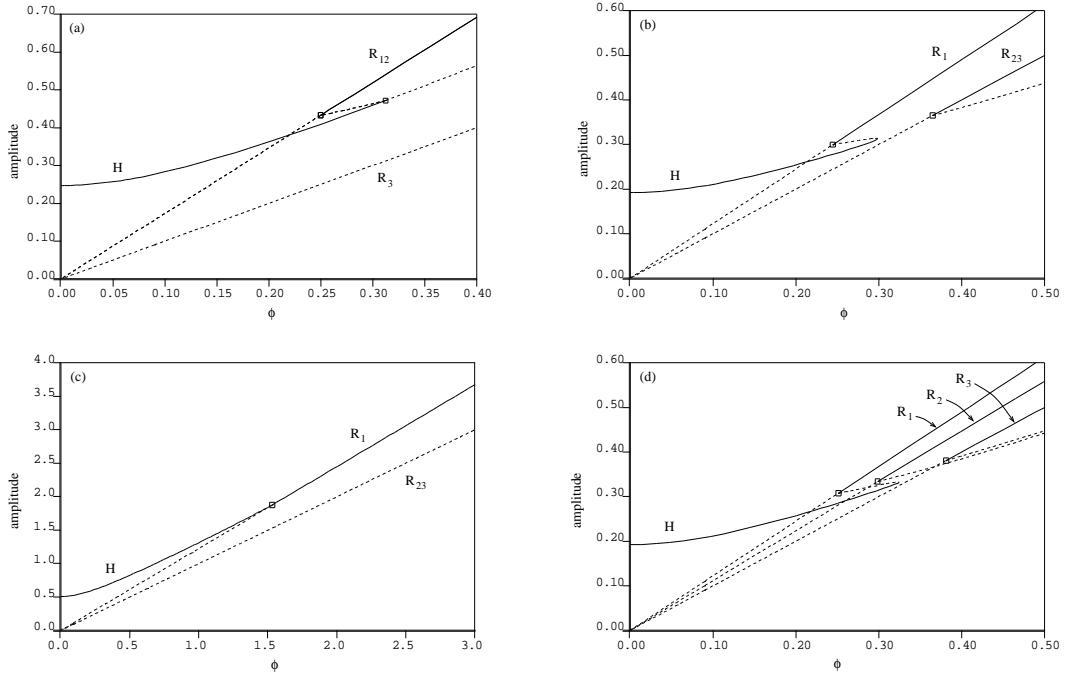


**Figure 3.8:** Bifurcation diagrams for  $r = 0$  and variable  $\phi$ . The amplitude  $(|z_1|^2 + |z_2|^2 + |z_3|^2)^{1/2}$  is plotted against  $\phi$  for (a)  $\beta = A_1 = A_2 = 3$  (corresponding to  $\theta = 0^\circ$ ); (b)  $\beta = 4$ ,  $A_1 = 1.5$ ,  $A_2 = 1$  (corresponding to  $\theta = 30^\circ$ ); (c)  $\beta = 1.2$ ,  $A_1 = 1.5$ ,  $A_2 = 1$  (also corresponding to  $\theta = 30^\circ$ ); (d)  $\beta = 4$ ,  $A_1 = 1.5$ ,  $A_2 = 1.25$  (corresponding to  $0^\circ < \theta < 30^\circ$ ). (Note that for clarity, some of the unstable solution branches have been omitted.)

Bifurcation diagrams for a number of values of  $\beta$ ,  $A_1$  and  $A_2$ , produced with the program AUTO (Doedel, 1981), are shown in Figure 3.8. We see that the three roll modes do indeed bifurcate from  $\phi = 0$ , and that they are all unstable initially. It is possible for them to become stable for larger  $\phi$  (at pitchfork bifurcations). The conditions for stable rolls are given in Table 3.1; these can be obtained from (3.14) using the equation  $\mu_j = A_j\phi^2$ . Note that  $R_1$  rolls are always stable for  $\phi$  large enough, while  $R_2$  and  $R_3$  may or may not become stable.

For the hexagons, there are two qualitatively different cases, depending on  $\theta$ . The case  $\theta = 0^\circ$  (corresponding to  $A_1 = A_2$ ), illustrated in Figure 3.8(a), is special. In this case the hexagon branch joins onto an unstable branch of ‘mixed modes’, which then connects back to the  $R_{12}$  branch; there is always hysteresis between rolls and hexagons for this value of  $\theta$ . The general case is  $\theta \neq 0$  (or  $A_1 \neq A_2$ ), corresponding to Figures 3.8(b)–3.8(d). Here the hexagons always connect to the  $R_1$  branch at the point where the latter becomes stable (this is the pitchfork bifurcation  $\phi = \phi_{\text{pf}}$  in the notation of Table 3.1). This pitchfork can be either supercritical (Figure 3.8c) or subcritical (Figures 3.8b and 3.8d). In the supercritical case, there is no possibility of hysteresis, but in the subcritical case, the hexagon branch turns around at a saddle-node bifurcation, and there is hysteresis between rolls and hexagons. We have not been able to find analytically the position of this saddle-node bifurcation, and so we cannot give a formula for the ‘amount’ of hysteresis, i.e. the width of the interval in  $\phi$  for which there is bistability, although we find that this interval tends to be widest when  $\beta$  is small (close to 1), or when the three  $A_j$  are close together in value.

In the specific case of  $\theta = 30^\circ$  (where  $A_2 = 1$ ), we can determine analytically whether the bifurcation is supercritical or subcritical. First compute  $A_c$  by the following formula:

$$\frac{1}{A_c} = \beta + \frac{2(1 + \beta - 2\beta^2)}{2\beta + \sqrt{2\beta + 2}}. \quad (3.15)$$

If  $A_c$  is negative, then the bifurcation is subcritical. If  $A_c$  is positive, then the bifurcation is supercritical for  $A_1 > A_c$ , or subcritical for  $A_1 < A_c$ . (The derivation of this condition is given in Appendix C.)

### Bifurcation diagrams varying both $r$ and $\phi$

Finally we consider the general case where both  $r$  and  $\phi$  are allowed to vary simultaneously. For simplicity we restrict our results to the cases  $\theta = 0^\circ$  and  $\theta = 30^\circ$ . In such cases two of the  $\mu_j$  will be equal; for example, we might have  $\mu_1 = \mu_2 = \mu$ , so that the

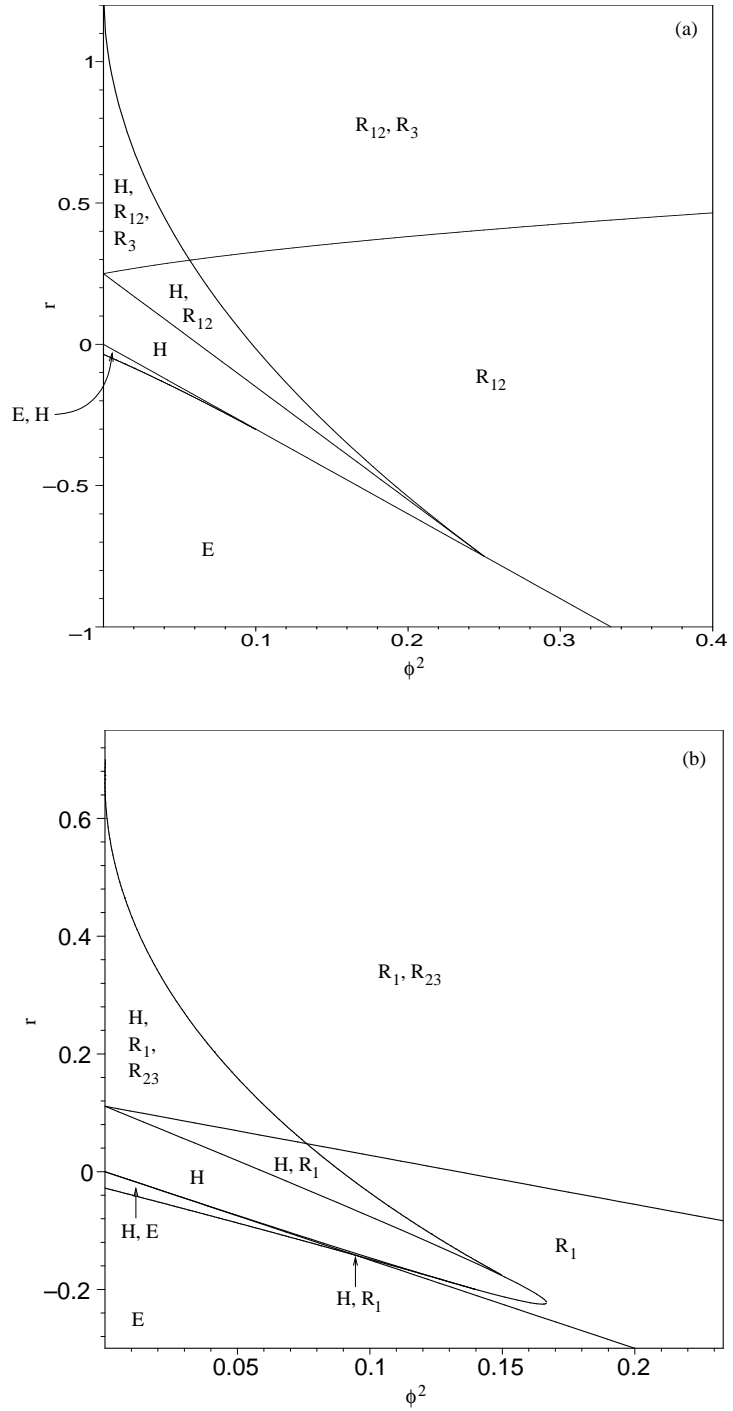


**Figure 3.9:** Diagrams showing the stability regions of rolls ( $R$ ), hexagons ( $H$ ) and the trivial (equilibrium) solution ( $E$ ) as functions of  $r$  and  $\phi$ , for (a)  $\beta = A_1 = A_2 = 3$ , corresponding to  $\theta = 0^\circ$ ; (b)  $\beta = 4, A_1 = 1.5, A_2 = 1$ , corresponding to  $\theta = 30^\circ$ .

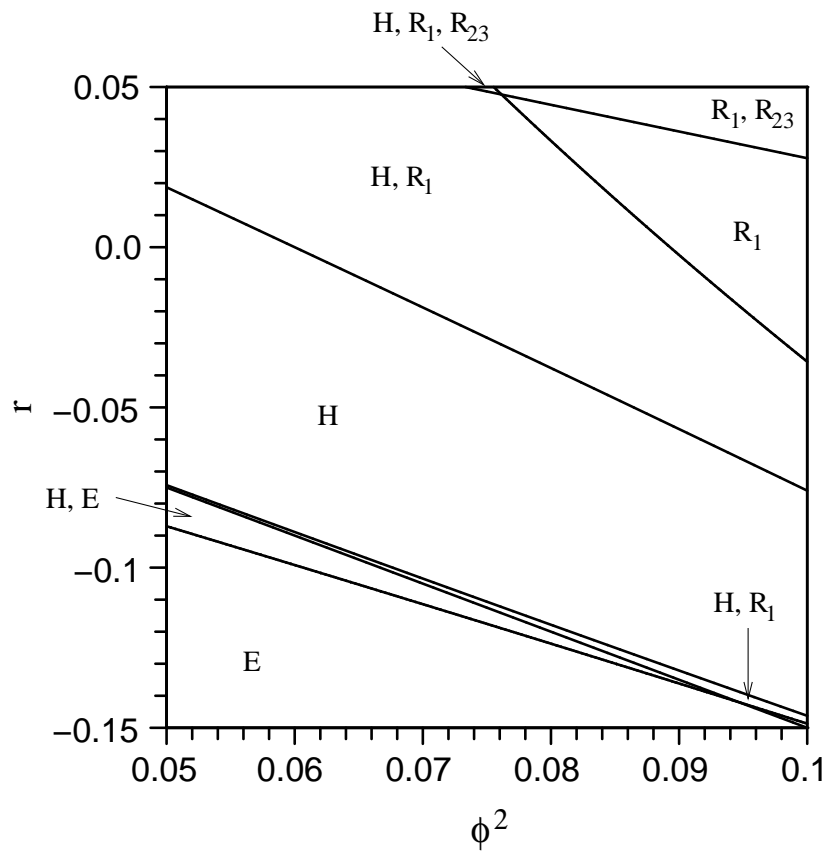


**Figure 3.10:** Close-up of part of Figure 3.9(b). Note the small region ‘H, R<sub>1</sub>’ near the bottom-right; this in fact extends upwards and leftwards all the way to the  $r$ -axis, although it does become extremely narrow as  $\phi \rightarrow 0$ .

two bifurcation parameters are  $\mu$  and  $\mu_3$ . These can be related to our parameters  $r$  and  $\phi$  by a simple change of variables. In such cases, Malomed et al. (1994) give plots of the stability regions in the  $\mu$ - $\mu_3$  plane. We can easily convert their results to the new coordinate system defined by  $r$  and  $\phi$  and thus produce diagrams of the stability regions of the various solutions in terms of  $r$  and  $\phi$ . See Figure 3.9, and also Figure 3.10, which is an enlargement of part of Figure 3.9(b).

The basic features of the diagrams are essentially independent of the parameters; although the sizes and positions of the stability regions can change, the topology seems to remain unaltered. We see rolls for large  $r$  or large  $\phi$ , with a region of stable hexagons for low  $\phi$  and intermediate  $r$ . In addition there is typically an area somewhere in parameter space of bistability between rolls and hexagons, indicating that hysteresis is a generic possibility, at least for some paths through parameter space.

Note that the bifurcation diagrams shown previously can be related to the graphs of Figure 3.9. For example, the diagrams of section 3.3.2, corresponding to the work of Matthews (1998), correspond on Figure 3.9 to moving upwards along the line  $\phi = \eta$  (where  $\eta$  is a small positive constant), a vertical line slightly to the right of the  $r$ -axis. Moving along this path on Figure 3.9(a), which corresponds to  $\theta = 0^\circ$ , would give the bifurcation diagram shown in Figure 3.7 (top panel). For Figure 3.9(b), corresponding to  $\theta = 30^\circ$ , the middle panel of Figure 3.7 would result. Note that in both cases the sequences of stable and unstable patterns shown in our diagram (Figure 3.9) agree with the work of Matthews (1998) (Figure 3.7). In the latter case, this is perhaps more difficult to see because of the small region near onset where rolls can be stable, visible on Figure 3.7 (middle panel) near  $\lambda_1 = \delta$ . On our diagram (Figure 3.9b) this in fact corresponds to the narrow wedge marked ‘ $H, R_1$ ’ which actually extends leftwards all the way to the  $\phi$ -axis; this can hopefully be seen more clearly on the enlargement shown in Figure 3.10.

The bifurcation diagrams of section 3.3.2, in which  $r = 0$  and  $\phi$  was varied, of course correspond to moving along the horizontal line  $r = 0$  on Figure 3.9. On Figure 3.9(a), this line moves from the region ‘ $H$ ’, to ‘ $H, R_{12}$ ’, and finally to ‘ $R_{12}$ ’; therefore, there is hysteresis between rolls and hexagons. Indeed there will always be such hysteresis, no matter what path one takes through parameter space, because the only way to move from region ‘ $H$ ’ to region ‘ $R_{12}$ ’ is via the region of bistability (except for the non-generic case in which one moves through the codimension-2 point at the very bottom right of the ‘ $H$ ’ region).

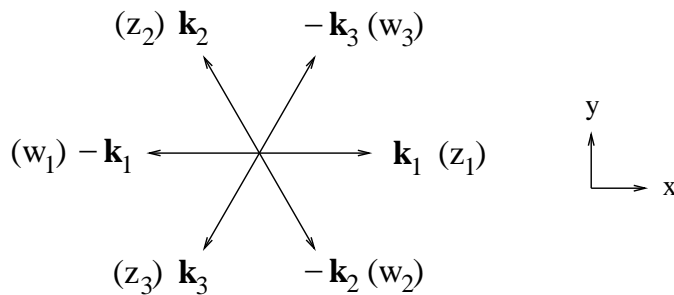


**Figure 3.11:** The wavevectors ( $\mathbf{k}_j$ ) and corresponding complex amplitudes ( $z_j$  and  $w_j$ ) used for the oscillatory hexagonal model. The arrows represent the direction of travel of each mode. As before, the direction of tilt of the magnetic field will be in the  $x$ -direction.

By contrast, on Figure 3.9(b), there are two distinct routes from the tongue-shaped ‘ $H$ ’ region to the ‘ $R_1$ ’ region. One involves going through the ‘side’ of the tongue, up and into the ‘ $H, R_1$ ’ region, and then into the ‘ $R_1$ ’ region. The other route goes through the ‘tip’ of the tongue at the far right-hand side, and thus goes directly into the ‘ $R_1$ ’ region without any hysteresis or bistability in between. Now, with the parameter values as chosen in Figure 3.9(b), the line  $r = 0$  takes the former route, going via a region of bistability before finally reaching the region where only rolls are stable. However, if different parameters are chosen, then the regions can shift around in such a way that the line  $r = 0$  moves through the ‘tip’ of the tongue rather than its ‘side’; this would correspond to the supercritical case mentioned in section 3.3.2, and there would be no hysteresis in this case. However, note that the region of bistability still exists – it has just been moved up to a higher value of  $r$ . Therefore, hysteresis could still be seen for these values of  $A_1$  and  $\beta$ , but one would have to move on a different path through parameter space, e.g. by varying  $\phi$  and fixing  $r$ , not at zero, but at some appropriate positive value; or indeed by fixing  $\phi$ , at an appropriate value, and varying  $r$ .

### 3.4 Oscillatory bifurcation on a hexagonal lattice

For small  $\zeta$  (and sufficiently large  $Q$ ), the initial bifurcation to convection is oscillatory rather than steady. This means that the representation (3.2) must be used instead of (3.1) for our solutions (with  $N = 3$  for the hexagonal lattice). The six modes, with complex amplitudes  $z_j$  and  $w_j$  ( $j = 1, 2, 3$ ), are shown in Figure 3.11.

Using the same approach as before, we can determine the most general set of am-

plitude equations for these six modes that are consistent with the symmetries of the problem. In the case of a vertical field, the relevant symmetry group is  $(T^2 \times D_6) \times S^1$ . ( $T^2$  and  $D_6$  have the same meanings as before; the extra symmetry  $S^1$  corresponds to a time shift symmetry, which essentially comes about because  $t$  now explicitly appears in the representation (3.2)). The amplitude equations consistent with this symmetry group are (Roberts et al., 1986):

$$\dot{z}_1 = [\mu + a|z_1|^2 + b|w_1|^2 + c(|z_2|^2 + |z_3|^2) + d(|w_2|^2 + |w_3|^2)]z_1 + f(z_2w_2 + z_3w_3)\bar{w}_1 \quad (3.16)$$

$$\dot{z}_2 = [\mu + a|z_2|^2 + b|w_2|^2 + c(|z_3|^2 + |z_1|^2) + d(|w_3|^2 + |w_1|^2)]z_2 + f(z_3w_3 + z_1w_1)\bar{w}_2 \quad (3.17)$$

$$\dot{z}_3 = [\mu + a|z_3|^2 + b|w_3|^2 + c(|z_1|^2 + |z_2|^2) + d(|w_1|^2 + |w_2|^2)]z_3 + f(z_1w_1 + z_2w_2)\bar{w}_3 \quad (3.18)$$

$$\dot{w}_1 = [\mu + a|w_1|^2 + b|z_1|^2 + c(|w_2|^2 + |w_3|^2) + d(|z_2|^2 + |z_3|^2)]w_1 + f(z_2w_2 + z_3w_3)\bar{z}_1 \quad (3.19)$$

$$\dot{w}_2 = [\mu + a|w_2|^2 + b|z_2|^2 + c(|w_3|^2 + |w_1|^2) + d(|z_3|^2 + |z_1|^2)]w_2 + f(z_3w_3 + z_1w_1)\bar{z}_2 \quad (3.20)$$

$$\dot{w}_3 = [\mu + a|w_3|^2 + b|z_3|^2 + c(|w_1|^2 + |w_2|^2) + d(|z_1|^2 + |z_2|^2)]w_3 + f(z_1w_1 + z_2w_2)\bar{z}_3 \quad (3.21)$$

Here,  $\mu$  is the (complex) linear growth rate, and  $a$ ,  $b$ ,  $c$ ,  $d$  and  $f$  are complex constants. Note that there are no quadratic terms in the oscillatory case, even when the up-down symmetry is broken. (This is a consequence of the extra time shift symmetry.)

Roberts et al. (1986) found eleven branches of solutions to these equations, which are listed in Table 3.2. Note that not all of these solutions will be found to be stable in our model (more on this below).

Figures 3.12 and 3.13 show graphical depictions of some of the solutions. These plots are obtained from the six amplitudes by using equation (3.2). Note that the solutions are functions of time: for the solutions shown in Figure 3.12, the only time-dependence is that the pattern travels with a constant speed, while for the patterns in Figure 3.13, there is a more complicated time-dependence and we have plotted snapshots at various time points. The time is expressed in units such that the period of the solution is 1. Only the first half of this period is plotted; the second half (from  $t = 1/2$  to  $t = 1$ ) is the same as the first half (from  $t = 0$  to  $t = 1/2$ ), but with a sign change.

<i>Solution</i>	<i>Label</i>	<i>Amplitudes</i>
oscillating triangles	OT	$(r, r, r, 0, 0, 0)$
standing hexagons	SHe	$(r, r, r, r, r, r)$
standing rectangles	SRe	$(0, r, r, 0, r, r)$
standing regular triangles	SRT	$(r, r, r, -r, -r, -r)$
standing rolls	SRo	$(r, 0, 0, r, 0, 0)$
travelling rectangles (1)	TRe1	$(r, 0, r, 0, 0, 0)$
travelling rectangles (2)	TRe2	$(r, 0, 0, 0, 0, r)$
travelling rolls	TRo	$(r, 0, 0, 0, 0, 0)$
twisted rectangles	TwRe	$(r, re^{2\pi i/3}, re^{4\pi i/3}, r, re^{2\pi i/3}, re^{4\pi i/3})$
wavy rolls (1)	WR1	$(r, 0, r, r, 0, -r)$
wavy rolls (2)	WR2	$(r, re^{2\pi i/3}, re^{4\pi i/3}, -r, -re^{2\pi i/3}, -re^{4\pi i/3})$

**Table 3.2:** The solutions found by Roberts et al. (1986) to equations (3.16)–(3.21), together with typical values for the amplitudes  $(z_1, z_2, z_3, w_1, w_2, w_3)$  ( $r$  represents a real number).

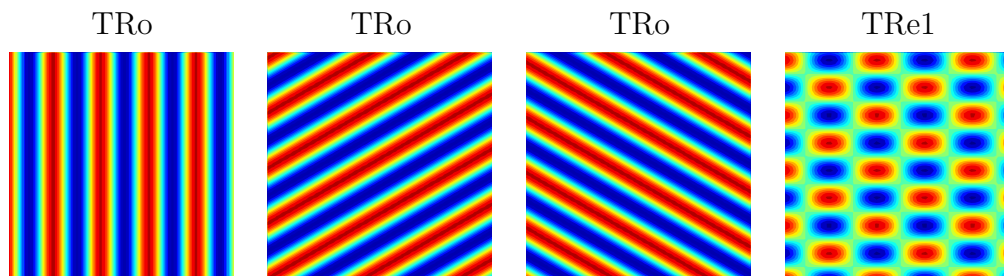


**Figure 3.12:** Solutions to equations (3.16)–(3.21). The TRo travel in a direction perpendicular to the roll axes; the TRe1 branch shown travels in the  $x$ -direction.

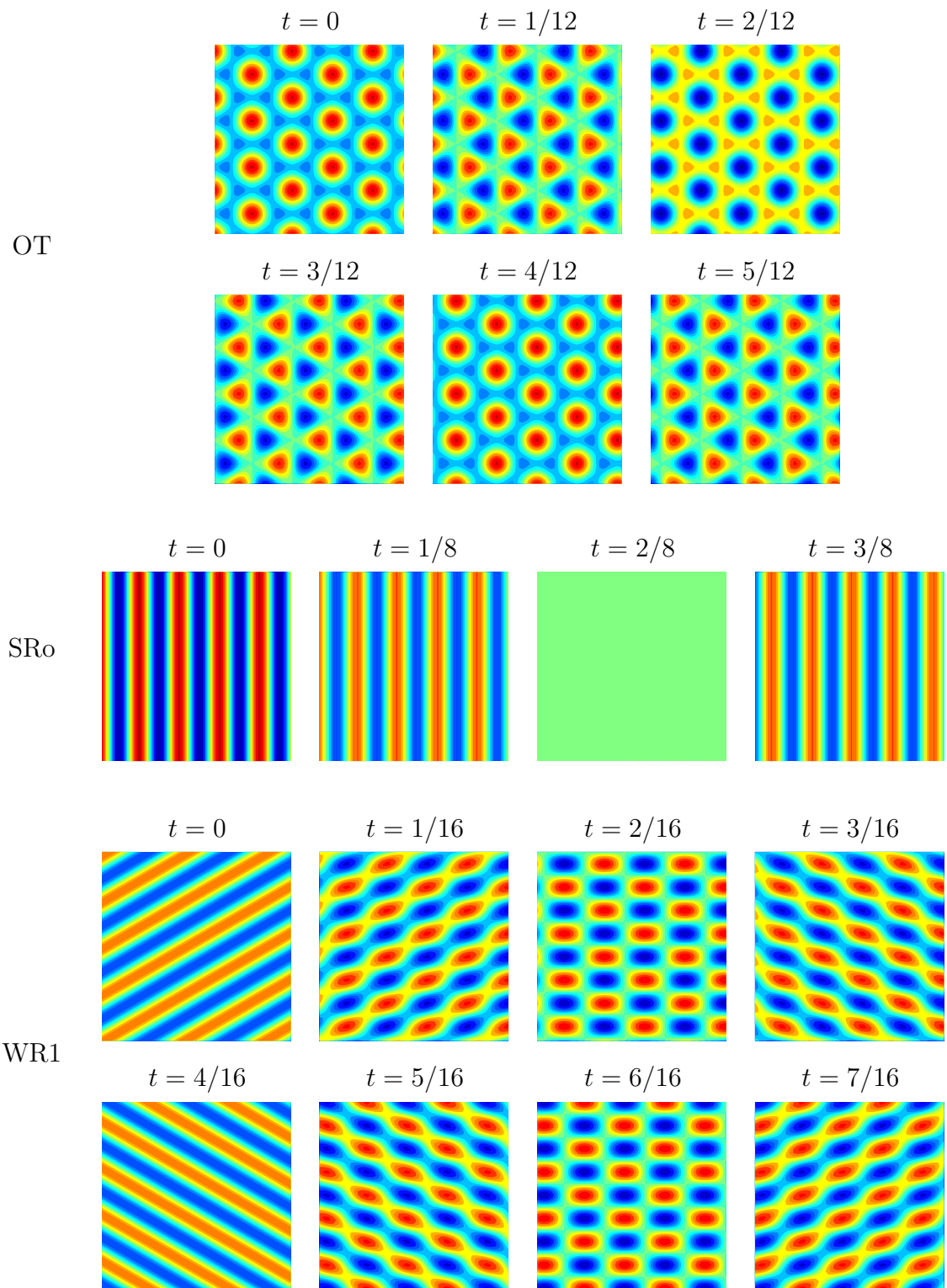


**Figure 3.13:** Solutions to equations (3.16)–(3.21).

### 3.4.1 An additional solution branch

In finding the above solutions, Roberts et al. (1986) used the equivariant Hopf theorem, which is an effective method, although it has the drawback that it is not guaranteed to find all possible solutions. We have taken a more elementary approach, simply by inspecting the equations in various cases (the full details are given in Appendix C). Our method still does not find all possible solutions, but we do find the eleven solution branches found by Roberts et al. (1986), plus one additional solution. This new solution does not have a one-complex-dimensional fixed point subspace, which is why it was not encountered by Roberts et al. (1986).

This new solution has the following form:

$$z_1 = z_2 \neq 0; \quad w_3 \neq 0; \quad z_3 = w_1 = w_2 = 0 \quad (3.22)$$

$$|z_1|^2 = \frac{\mu_r(d_r - a_r)}{a_r^2 - 2d_r^2 + a_r c_r} \quad (3.23)$$

$$|w_3|^2 = \frac{\mu_r(2d_r - a_r - c_r)}{a_r^2 - 2d_r^2 + a_r c_r} \quad (3.24)$$

$$\frac{d}{dt}(\arg z_1) = \mu_i + (a_i + c_i)|z_1|^2 + d_i|w_3|^2 \quad (3.25)$$

$$\frac{d}{dt}(\arg w_3) = \mu_i + a_i|w_3|^2 + 2d_i|z_1|^2. \quad (3.26)$$

These equations, together with stability criteria for the solution, are derived in Appendix C. Unfortunately it is not possible to write down the stability conditions in a simple form; however, it is a straightforward matter to compute the stability eigenvalues numerically. We have found that the solution is often unstable, but it is stable for (at least) the following choice of parameters:  $a = -1$ ,  $b = -1.5$ ,  $c = -0.2$ ,  $d = -0.3$  and  $f = -0.1$  (for which  $|z_1| = |z_2| = 0.828\sqrt{\mu_r}$  and  $|w_3| = 0.767\sqrt{\mu_r}$ ). We have confirmed this result by numerically solving (3.16)–(3.21) as an initial value problem; one such run is shown in Figure 3.14, which demonstrates the existence and stability of the solution in this case.

The solution in this case is shown in Figure 3.15. Note that it resembles the oscillating triangle solution, albeit with a slight asymmetry (since  $|z_1|$  and  $|w_3|$  take slightly different values). The difference is that as well as oscillating between regular hexagons and regular triangles, the new solution also appears to drift (upwards and rightwards in the case shown in Figure 3.15). The other main difference is that the OT solution oscillates between hexagons and triangles much more quickly (in fact, three times more quickly)

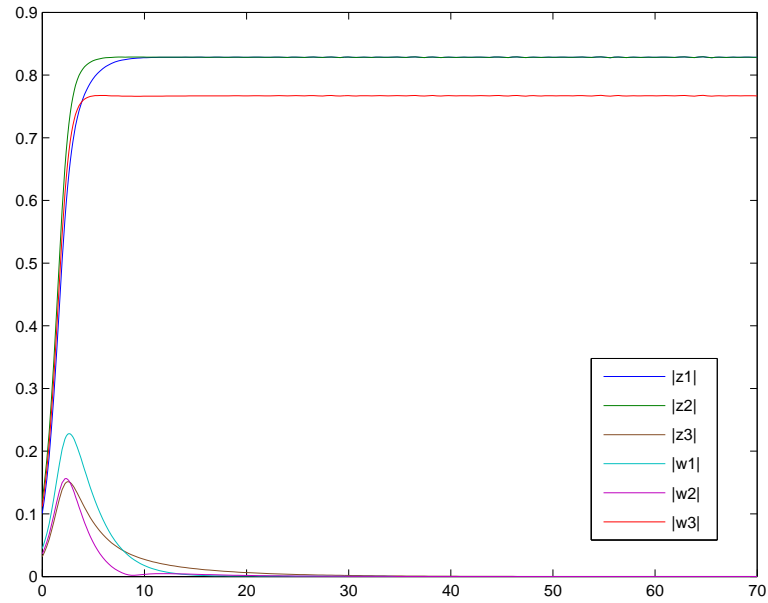


**Figure 3.14:** Numerical solution of (3.16)–(3.21), illustrating the existence and stability of the new solution branch. The six amplitudes  $|z_1|$ ,  $|z_2|$ ,  $|z_3|$ ,  $|w_1|$ ,  $|w_2|$  and  $|w_3|$  are plotted against time. (The parameters were:  $a = -1$ ,  $b = -1.5$ ,  $c = -0.2$ ,  $d = -0.3$  and  $f = -0.1$ , with  $\mu = 1$ .)

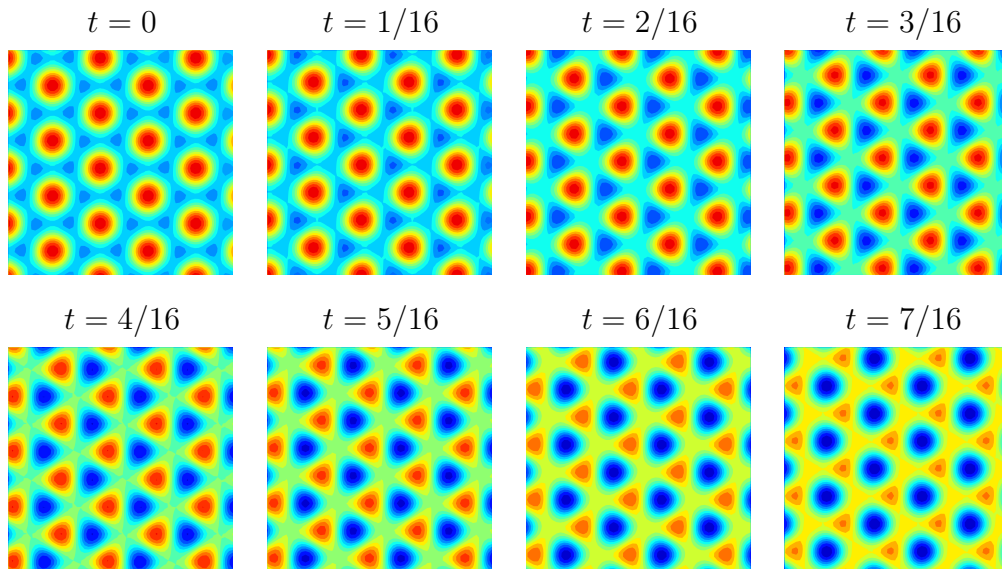


**Figure 3.15:** The new ‘drifting oscillating triangles’ solution.

than this new solution does, as can be seen by comparing the relevant figures. (In terms of symmetries, the oscillating triangles have a spatiotemporal symmetry consisting of a time shift of  $1/3$  of the total period together with a translation; the new ‘drifting oscillating triangles’ actually have no spatiotemporal symmetries.)

We have not considered what happens to this solution when the equations are truncated at higher order than third order. A version of equations (3.27)–(3.32) truncated at fifth order, instead of third, is given by Roberts et al. (1986) (see their Proposition 2.2). These equations contain non-zero terms at fifth order in the equations for  $\dot{z}_3$ ,  $\dot{w}_1$  and  $\dot{w}_2$  (these are the three variables that are zero in our third-order solution). Therefore, the solution at higher order will have small (rather than identically zero) values for  $z_3$ ,  $w_1$  and  $w_2$ ; this might cause the solution to have slightly different properties (although we have not investigated this in detail).

The reason that Roberts et al. (1986) did not find this new solution branch is that it does not have maximal isotropy. In fact, the only symmetry possessed by the new solution is the reflection symmetry that exchanges  $z_1$  and  $z_2$ , and  $w_1$  and  $w_2$ . None of the other elements of  $D_6$  are symmetries, nor are there any spatiotemporal symmetries. Therefore the isotropy subgroup of this solution is just  $Z_2$ . The corresponding fixed point set is  $(z_1, z_2, z_3, w_1, w_2, w_3) = (p, p, q, r, r, s)$  (where  $p$ ,  $q$ ,  $r$  and  $s$  are arbitrary complex numbers) which is 4-D complex; a 1-D complex fixed point set would have been needed for the solution to be detectable via the usual methods (the equivariant Hopf theorem).

### 3.4.2 Weakly broken symmetry

We would now like to investigate non-vertical magnetic fields, and we (once again) do this by weakly breaking the isotropy, introducing a small tilt angle  $\phi$ . As before, we

break the symmetry in the linear terms only, leading to:

$$\dot{z}_1 = [\mu_1 + a|z_1|^2 + b|w_1|^2 + c(|z_2|^2 + |z_3|^2) + d(|w_2|^2 + |w_3|^2)]z_1 + f(z_2w_2 + z_3w_3)\bar{w}_1 \quad (3.27)$$

$$\dot{z}_2 = [\mu_2 + a|z_2|^2 + b|w_2|^2 + c(|z_3|^2 + |z_1|^2) + d(|w_3|^2 + |w_1|^2)]z_2 + f(z_3w_3 + z_1w_1)\bar{w}_2 \quad (3.28)$$

$$\dot{z}_3 = [\mu_3 + a|z_3|^2 + b|w_3|^2 + c(|z_1|^2 + |z_2|^2) + d(|w_1|^2 + |w_2|^2)]z_3 + f(z_1w_1 + z_2w_2)\bar{w}_3 \quad (3.29)$$

$$\dot{w}_1 = [\mu'_1 + a|w_1|^2 + b|z_1|^2 + c(|w_2|^2 + |w_3|^2) + d(|z_2|^2 + |z_3|^2)]w_1 + f(z_2w_2 + z_3w_3)\bar{z}_1 \quad (3.30)$$

$$\dot{w}_2 = [\mu'_2 + a|w_2|^2 + b|z_2|^2 + c(|w_3|^2 + |w_1|^2) + d(|z_3|^2 + |z_1|^2)]w_2 + f(z_3w_3 + z_1w_1)\bar{z}_2 \quad (3.31)$$

$$\dot{w}_3 = [\mu'_3 + a|w_3|^2 + b|z_3|^2 + c(|w_1|^2 + |w_2|^2) + d(|z_1|^2 + |z_2|^2)]w_3 + f(z_1w_1 + z_2w_2)\bar{z}_3 \quad (3.32)$$

Recall that once  $\phi$  becomes non-zero, the orientation of the lattice is important. For simplicity, we have restricted ourselves to one particular orientation, as illustrated in Figure 3.11. We have picked  $\mathbf{k}_1$  to lie on the  $x$ -axis; this corresponds to perpendicular rolls, which are the most unstable mode for small  $\phi$  (as shown in the previous chapter), so we are including the most unstable mode plus five other modes. We then have the following form for the growth rates for small  $r$  and small  $\phi$ :

$$\mu_1 = \gamma r - \alpha \phi \quad (3.33)$$

$$\mu_2 = \mu_3 = \gamma r + \beta \phi \quad (3.34)$$

$$\mu'_1 = \gamma r + \alpha \phi \quad (3.35)$$

$$\mu'_2 = \mu'_3 = \gamma r - \beta \phi \quad (3.36)$$

where  $\alpha$ ,  $\beta$  and  $\gamma$  are complex constants. Here we have scaled both  $r$  and  $\phi$  as  $O(\epsilon)$  and expanded the growth rates to first order in  $\epsilon$ . All the terms in equations (3.27)–(3.32) are now of order  $\epsilon^3$ .

Before proceeding, we briefly discuss the effects that the symmetry-breaking has on the solutions. As in the steady case, once the symmetry is broken we find that many of the solution branches ‘split’ into two or more separate branches, that previously were related by symmetry, but now are genuinely different solutions. These are summarized in Table 3.3. For example, there are now four different branches of travelling rolls (labelled

<i>Solution</i>	<i>Label</i>	<i>Amplitudes</i>
travelling rolls	TRo(a)	$(0, 0, 0, x, 0, 0)$
	TRo(b)	$(0, x, 0, 0, 0, 0)$ or $(0, 0, x, 0, 0, 0)$
	TRo(c)	$(0, 0, 0, 0, x, 0)$ or $(0, 0, 0, 0, 0, x)$
	TRo(d)	$(x, 0, 0, 0, 0, 0)$
standing rolls	SRo(a)	$(x, 0, 0, y, 0, 0)$
	SRo(b)	$(0, x, 0, 0, y, 0)$ or $(0, 0, x, 0, 0, y)$
travelling rectangles (1)	TRe1(a)	$(0, x, x, 0, 0, 0)$
oscillating triangles	OT(a)	$(0, 0, 0, x, y, y)$
	OT(b)	$(x, y, y, 0, 0, 0)$
wavy rolls (1)	WR1(a)	$(0, x, x, 0, y, y)$

**Table 3.3:** *The solutions found to equations (3.27)–(3.32) and typical forms of the amplitudes  $(|z_1|, |z_2|, |z_3|, |w_1|, |w_2|, |w_3|)$  in each case. (Here,  $x$  and  $y$  represent real numbers. More details on the exact form of each solution branch can be found in Appendix C.) Only solutions that are found to be stable (in the analysis below) have been shown. Note that there are multiple forms of some of the solution branches, because of the asymmetry; these different forms have been indicated by lower-case letters, e.g. TRo(a–d).*

‘a’-‘d’), instead of just one. (There are not six, one for each  $z_j$  and each  $w_j$ , because we still have the  $y \rightarrow -y$  reflection symmetry; for example, ‘ $z_2$ -rolls’ and ‘ $z_3$ -rolls’ are still equivalent, but they are different to ‘ $z_1$ -rolls’.)

Figure 3.16 shows graphically how the symmetry breaking changes the appearance of some of the solution branches (compare this to Figure 3.13). Here we have broken the symmetry by taking  $|z_j|$  and  $|w_j|$  each to be slightly different, as follows:  $|w_1| = 1.6$ ,  $|z_2| = |z_3| = 1.3$ ,  $|w_2| = |w_3| = 1.0$ , and  $|z_1| = 0.7$ . (These values are to be substituted in place of  $x$  and  $y$  in Table 3.3.) The values have been chosen arbitrarily; they are intended purely to illustrate how the solutions change when the amplitudes are no longer all equal.

For SRO, the asymmetry means that the solution does not return to the ‘zero’ state at  $t = 2/8$  as it did before. For OT(a), the solutions start to look a little more like a perpendicular roll pattern (because of the dominance of that particular roll mode). For WR1, the solution no longer reaches a ‘pure’ roll state at each end of the oscillation. Note also that the asymmetry has no effect on the TRo or TRe1 solutions.

Returning to our amplitude equations, we can rescale  $\phi$  and  $r$  to ensure that  $\alpha_r = \gamma_r = 1$ , leaving  $\beta_r$ ,  $\alpha_i$ ,  $\beta_i$  and  $\gamma_i$  as free parameters. We can also rescale time and the amplitudes to remove two degrees of freedom from the choices of  $a$ ,  $b$ ,  $c$ ,  $d$  and  $f$ . Thus there are effectively 12 undetermined coefficients in the problem as well as the parameters  $r$  and  $\phi$ .

The coefficients  $a$ ,  $b$ ,  $c$ ,  $d$  and  $f$  present a problem, since they represent five complex parameters whose values cannot be determined from symmetry arguments alone. However, Clune and Knobloch (1994) have performed a perturbation analysis of the equations for Boussinesq magnetoconvection, using a vertical field and illustrative boundary conditions (magnetic field constrained to be vertical at top and bottom), and found the values of these coefficients for a wide range of  $Q$ ,  $\zeta$  and  $\sigma$  values.

Therefore, our approach will be to look at the patterns found by Clune and Knobloch (1994) to occur in magnetoconvection, and see how these change as one introduces a slightly tilted field. The most common pattern that they find is OT, and there are large regions of parameter space where this is the only stable solution. There are also fairly large regions where TRo are the only stable solution, and where OT and SRO are simultaneously stable.

Now suppose, for example, that we are in a situation where OT are the only stable pattern when  $\phi = 0$ , and we want to know what happens as  $\phi$  is increased above zero. To answer this we need to choose a set of values for  $a$ ,  $b$ ,  $c$  etc. that would lead to

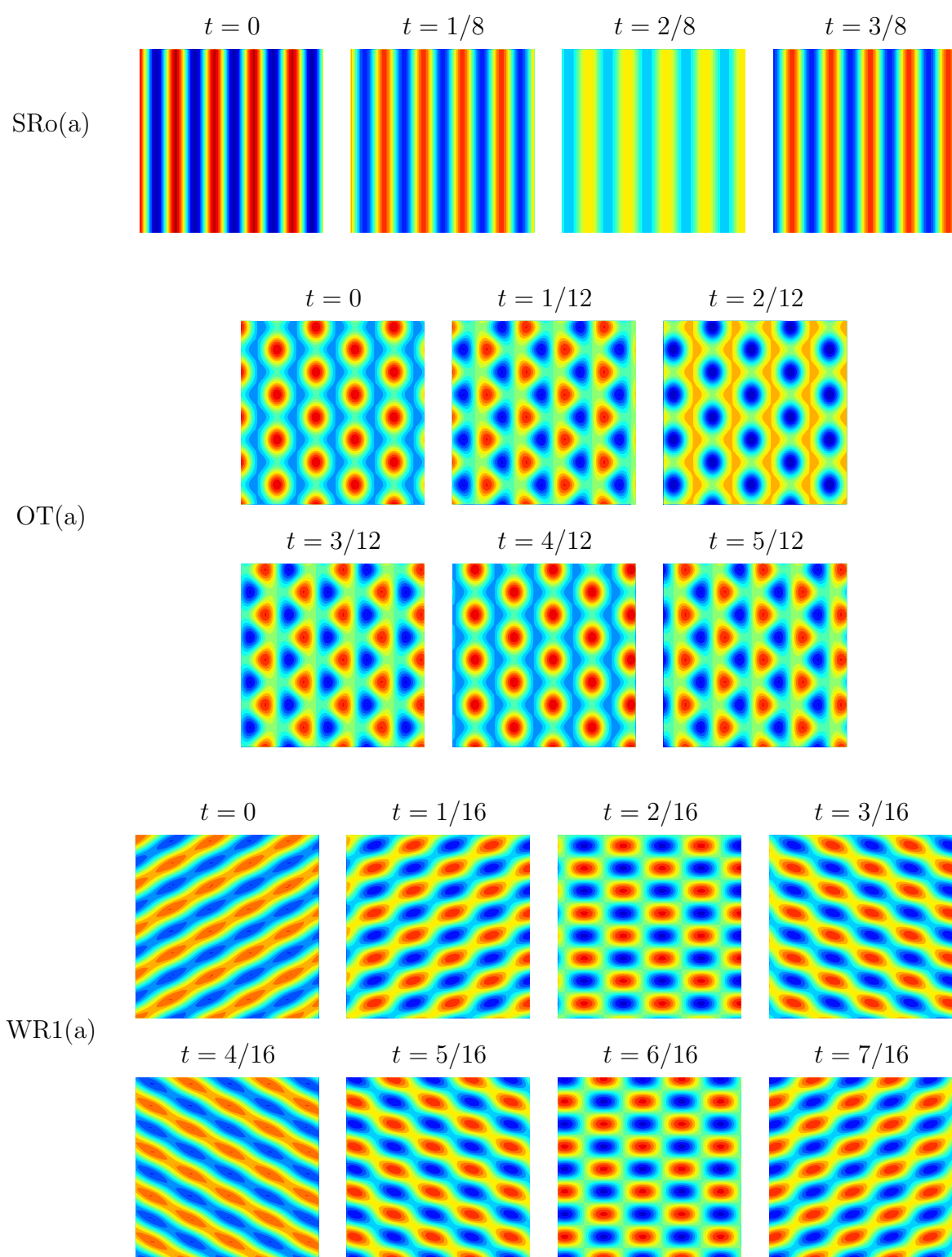


**Figure 3.16:** Solutions to equations (3.27)–(3.32).

<i>Case</i>	<i>a</i>	<i>b</i>	<i>c</i>	<i>d</i>	<i>f</i>	<i>Stable solutions</i>
						<i>in symmetric case</i>
(a)	$-1.5 + 2i$	$-3 + 2.2i$	$-3 + 0.5i$	$-3 + 0.8i$	$-1 - 2i$	TRo
(b)	$-10$	$-9.6$	$-1$	$-9.5$	$-4.2$	OT
(c)	$-3 - 1.1i$	$-1.5 + 0.3i$	$-1.7 + 0.7i$	$-4 + i$	$-1.8 + i$	SRo & OT

**Table 3.4:** *The values chosen for the nonlinear coefficients  $a$ ,  $b$ ,  $c$ ,  $d$  and  $f$ .*

such a situation. Unfortunately, this choice is far from unique; there are many such sets of values that would give OT as the only stable pattern when  $\phi$  is zero. We can only repeat our analysis for several different sets of parameter values, each having OT stable at  $\phi = 0$ , and try to determine which features of our results are robust. This can of course be done for other situations as well – we will also look at the cases where TRo are the only stable solution for  $\phi = 0$ , and where SRo and OT are the only stable solutions for  $\phi = 0$ .

One must also choose values for  $\alpha$ ,  $\beta$  and  $\gamma$ . We have chosen to investigate the particular values  $\beta_r = 0.65$ ,  $\alpha_i = 0.5$ ,  $\beta_i = 0.7$ ,  $\gamma_i = 0$  in detail. These have been chosen arbitrarily, but they illustrate the typical behaviour; the effects of changing these values will be discussed (briefly) below.

The results, showing the existence and stability regions for the various patterns, are shown in Figure 3.17. The values of the coefficients  $a$ ,  $b$ ,  $c$ ,  $d$  and  $f$  that were used in each case are given in Table 3.4. The boundaries of the existence and stability regions are always radial lines through the origin. It can be seen that for small  $\phi$  (or large  $r$ ), the stable patterns are the same as in the symmetric problem (as required), but for larger tilt angles new patterns can be made to appear. Generally speaking, one finds that TRo(a) usually become stable for the larger values of  $\phi$ . Note that TRo(a) corresponds to perpendicular rolls, which are the preferred mode in linear theory for  $\phi$  below the Lifshitz point. (The model in this section is valid only for small tilt angles, as has already been discussed. Therefore we never get into the regime where either oblique or parallel rolls become preferred in linear theory.) We also find that TRe1(a) are often (but not always) stable for large  $\phi$ , a situation illustrated by cases (b) and (c). In addition, when SRo and OT are both stable for small  $\phi$ , illustrated by case (c), wavy rolls of the first kind (WR1) can be stable for some regions of parameter space.

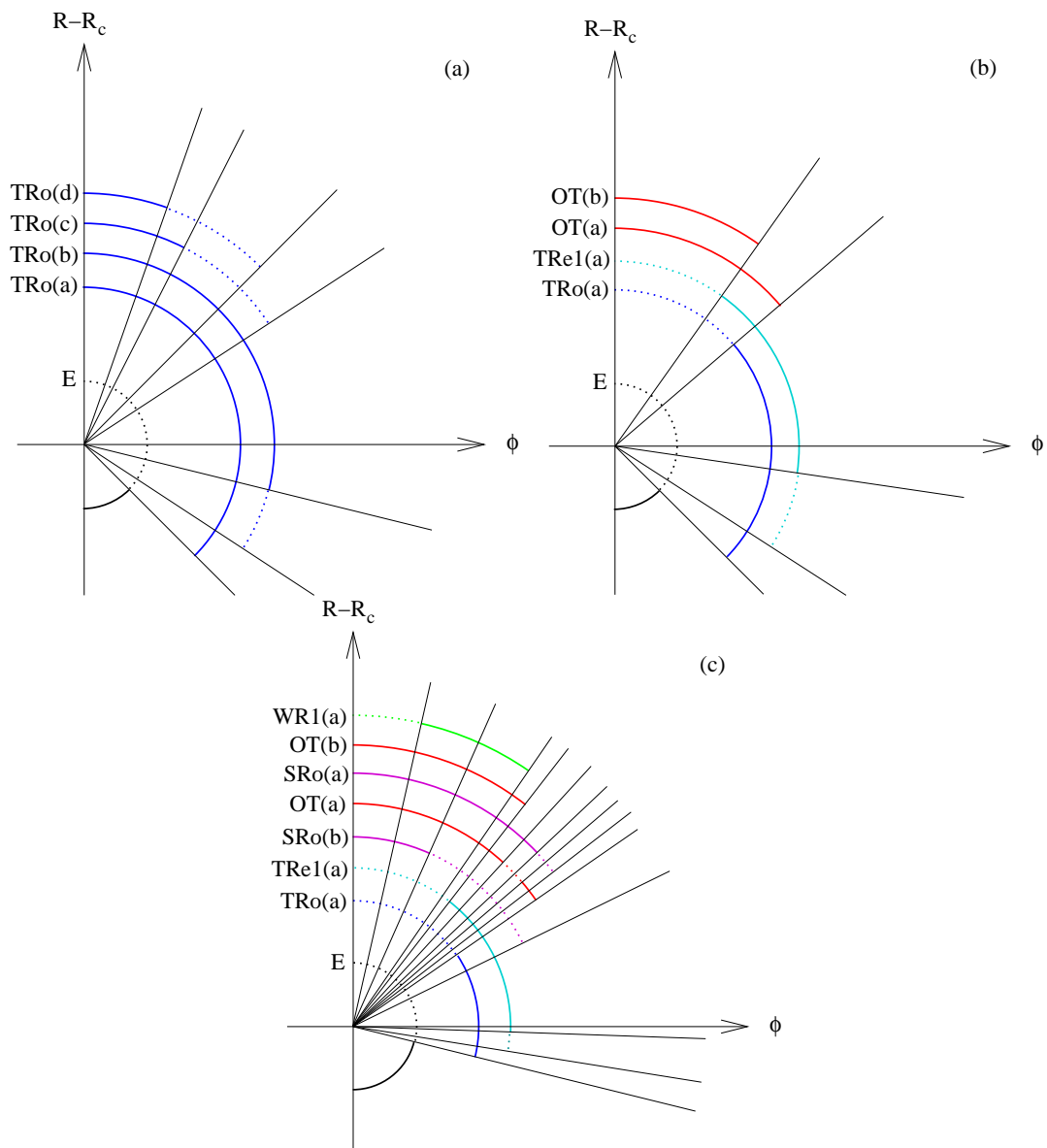


**Figure 3.17:** Results for the oscillatory hexagonal model. The coloured arcs represent the different solution branches; solid lines indicate a region where there is a stable solution, and dashed lines indicate an unstable solution. (The radial lines represent the bifurcations.) See text for further explanation.

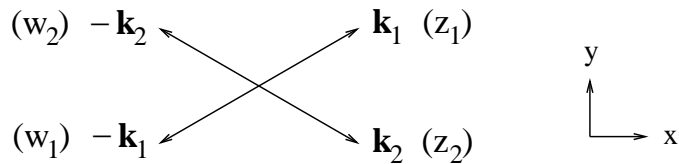


**Figure 3.18:** The four modes included in the rhombic lattice (showing the wavevectors and corresponding complex amplitudes). Note that the magnetic field is tilted in the  $x$ -direction (as usual).

Figures 3.17(a–c) were each produced with particular choices for the coefficients. We have, as explained above, also tried different values of the various parameters in order to check the robustness of the results. In cases where TRo are the only stable pattern at  $\phi = 0$ , it appears that the qualitative picture of Figure 3.17(a) is always found, whatever the particular parameter values chosen. In other cases, there can be some changes. The set of possible stable patterns always seems to remain the same, with the exception of TRel(a), which was found to be stable only in certain cases. However, the exact position of the bifurcation lines, and indeed the order in which those bifurcations are encountered as one moves around the origin, can vary depending on the precise parameter values chosen.

## 3.5 Oscillatory bifurcation on a rhombic lattice

Our final piece of work in this chapter will be to consider the oscillatory problem on a rhombic lattice instead of a hexagonal one. See Figure 3.18. The motivation for this choice of lattice comes from the linear theory, and in particular to the regime where oblique rolls are preferred. A rhombic lattice can include the two preferred modes (represented by  $z_1$  and  $z_2$ ) as well as their counterparts travelling in the opposite directions (represented by  $w_1$  and  $w_2$ ).

### 3.5.1 The symmetric case

The problem of oscillatory (Hopf) bifurcation on a rhombic lattice has been considered before, by Silber et al. (1992). Their work was motivated by studies of nematic liquid crystals, but it is not restricted only to liquid crystals; rather, it can be applied to any system possessing the same symmetries. (The problem has the symmetry group  $T^2 \rtimes D_2$ , which consists of  $x$  and  $y$  translations plus the discrete symmetries of the

rhombic lattice.)

Silber et al. (1992) obtained the following equations, truncated at third order, for the evolution of the amplitudes  $z_1$ ,  $z_2$ ,  $w_1$  and  $w_2$ :

$$\dot{z}_1 = \mu z_1 + (a|z_1|^2 + b|w_2|^2 + c|w_1|^2 + d|z_2|^2)z_1 + fw_2z_2\bar{w}_1 \quad (3.37)$$

$$\dot{z}_2 = \mu z_2 + (a|z_2|^2 + b|w_1|^2 + c|w_2|^2 + d|z_1|^2)z_2 + fw_1z_1\bar{w}_2 \quad (3.38)$$

$$\dot{w}_1 = \mu w_1 + (a|w_1|^2 + b|z_2|^2 + c|z_1|^2 + d|w_2|^2)w_1 + fw_2z_2\bar{z}_1 \quad (3.39)$$

$$\dot{w}_2 = \mu w_2 + (a|w_2|^2 + b|z_1|^2 + c|z_2|^2 + d|w_1|^2)w_2 + fw_1z_1\bar{z}_2 \quad (3.40)$$

The coefficient  $\mu$  is the (complex) linear growth rate. The coefficients  $a$ ,  $b$ ,  $c$ ,  $d$  and  $f$  are also complex, and depend on the physical properties of the system; their values cannot be determined by symmetry arguments alone.

These five undetermined complex coefficients are problematic, since they essentially represent ten free parameters in the model. Fortunately, however, there is a limit in which some of them can be eliminated; this occurs when the angle of obliquity of the oblique rolls is small, i.e. the angle of the wavevectors  $\mathbf{k}_1$  and  $\mathbf{k}_2$  to the  $x$ -axis is small. This situation occurs close to the so-called Lifshitz point, the point where oblique rolls first appear (see previous chapter). In such circumstances an oblique roll can be represented as a slow modulation of a perpendicular roll.

Silber et al. (1992) performed a calculation using exactly this method, writing a general superposition of leftward- and rightward-travelling rolls as

$$\epsilon^{1/2}[A(X, Y, T)e^{i(kx-\omega t)} + B(X, Y, T)e^{i(-kx-\omega t)}] + \text{c.c.} \quad (3.41)$$

(to lowest order in  $\epsilon$ ), where the scalings are  $X = \epsilon^{1/2}x$ ,  $Y = \epsilon^{1/4}y$  and  $T = \epsilon t$ , and  $\epsilon$  is a small parameter, proportional to the distance from the Hopf bifurcation. Here, solutions independent of  $Y$  indicate perpendicular rolls, while solutions depending on both  $X$  and  $Y$  indicate perpendicular rolls.

Using the symmetries of the problem, Silber et al. (1992) obtain the following evolution equations for  $A$  and  $B$ :

$$\begin{aligned} \frac{\partial A}{\partial T} = & c\frac{\partial A}{\partial X} + d\frac{\partial^2 A}{\partial X^2} + s\frac{\partial^2 A}{\partial Y^2} + g\frac{\partial^3 A}{\partial X\partial Y^2} - h\frac{\partial^4 A}{\partial Y^4} + rA \\ & + \alpha(|A|^2 + |B|^2)A + \beta|A|^2A \end{aligned} \quad (3.42)$$

$$\begin{aligned} \frac{\partial B}{\partial T} = & -c\frac{\partial B}{\partial X} + d\frac{\partial^2 B}{\partial X^2} + s\frac{\partial^2 B}{\partial Y^2} - g\frac{\partial^3 B}{\partial X\partial Y^2} - h\frac{\partial^4 B}{\partial Y^4} + rB \\ & + \alpha(|B|^2 + |A|^2)B + \beta|B|^2B, \end{aligned} \quad (3.43)$$

where  $c$  and  $r$  are real and all other coefficients are complex. The trivial solution ( $A = B = 0$ ) is unstable to perturbations with wavevector  $(Q_c, P_c)$  if  $r > r_c$ , where

$$\begin{aligned} Q_c = 0, \quad P_c = 0, \quad r_c = 0 & \quad \text{if } s_r > 0 \\ Q_c = \frac{g_i P_c^2}{2d_r}, \quad P_c^2 = \frac{2d_r s_r}{g_i^2 - 4h_r d_r}, \quad r_c = \frac{s_r P_c^2}{2} < 0 & \quad \text{if } s_r < 0 \end{aligned} \quad (3.44)$$

Therefore, we see that the Lifshitz point is represented by  $s_r = 0$ . In other words,  $s_r$  depends on  $\phi$ , with  $s_r > 0$  if  $\phi$  is below the Lifshitz point, where perpendicular rolls are found, while  $s_r < 0$  if  $\phi$  is above the Lifshitz point, where oblique rolls are found. (Note that we must assume  $4h_r d_r > g_i^2$  in order for the model to give oblique solutions.)

In the oblique case ( $s_r < 0$ ), we can relate the equations for  $A$  and  $B$  back to the amplitudes  $z_1, z_2, w_1$  and  $w_2$  by making the following substitution:

$$A = e^{iQ_c X} [z_1(T)e^{iP_c Y} + z_2(T)e^{-iP_c Y}] \quad (3.45)$$

$$B = e^{-iQ_c X} [w_2(T)e^{iP_c Y} + w_1(T)e^{-iP_c Y}] \quad (3.46)$$

If higher order harmonics are neglected, then first order ODEs can be obtained for the four complex amplitudes. These are of the form of (3.37)–(3.40) (as indeed they must be by symmetry arguments), but this time we know the values of the coefficients  $a, b, c, d$  and  $f$  (in terms of  $\alpha$  and  $\beta$ ), as follows:

$$d = 2a = 2(\alpha + \beta), \quad c = f = b = \alpha. \quad (3.47)$$

It may seem that we are no better off, since we still do not know the values of  $\alpha$  and  $\beta$ . However, by using (3.47) we can in fact eliminate  $c, d,$  and  $f$  from (3.37)–(3.40) in favour of  $a$  and  $b$ .

Therefore, by assuming that we are close to the Lifshitz point ( $\phi$  only just above  $\phi_c$ ), the problem is greatly simplified, since in this limit there are only two undetermined coefficients instead of five.

### 3.5.2 Weakly broken symmetry

The problem considered so far contains a left-right reflection symmetry, which is valid for a vertical magnetic field, but not for an inclined one. As usual, we will deal with this by weakly breaking the symmetry; we write  $\mu'$  instead of  $\mu$  in equations (3.39) and (3.40), while leaving equations (3.37) and (3.38) unchanged. As before, the nonlinear coefficients are not modified. If we assume that we are close to the Lifshitz point, so

that (3.47) applies, then we are left with the following system of equations:

$$\dot{z}_1 = \mu z_1 + (a|z_1|^2 + b|w_2|^2 + b|w_1|^2 + 2a|z_2|^2)z_1 + bw_2 z_2 \bar{w}_1 \quad (3.48)$$

$$\dot{z}_2 = \mu z_2 + (a|z_2|^2 + b|w_1|^2 + b|w_2|^2 + 2a|z_1|^2)z_2 + bw_1 z_1 \bar{w}_2 \quad (3.49)$$

$$\dot{w}_1 = \mu' w_1 + (a|w_1|^2 + b|z_2|^2 + b|z_1|^2 + 2a|w_2|^2)w_1 + bw_2 z_2 \bar{z}_1 \quad (3.50)$$

$$\dot{w}_2 = \mu' w_2 + (a|w_2|^2 + b|z_1|^2 + b|z_2|^2 + 2a|w_1|^2)w_2 + bw_1 z_1 \bar{z}_2 \quad (3.51)$$

We now consider conditions under which the assumption of weakly broken symmetry is valid. Note that we cannot use our previous tactic of assuming small  $\phi$ ; this is because we have already assumed that we are near to the Lifshitz point, which corresponds to taking  $\phi$  just above the value where oblique rolls first appear, a value that is not necessarily small.

Instead, we recall that with our choice of boundary conditions, there is a left-right reflection symmetry in the problem when  $\kappa$  does not vary with depth, even when  $\phi$  is non-zero. Therefore, if we take  $\delta$  to be some measure of  $|\mathrm{d}\kappa/\mathrm{d}z|$ , then the symmetry-breaking will be proportional to  $\delta$ . If we also take  $r$  to be the bifurcation parameter  $(R - R_c)/R_c$ , then we have the following form for  $\mu$  and  $\mu'$  (at lowest order):

$$\mu = r - \delta; \quad \mu' = r + \delta. \quad (3.52)$$

The obvious scaling to take is  $r \propto \epsilon^2$ ,  $\delta \propto \epsilon^2$ , with  $|z_j|$  and  $|w_j|$  of order  $\epsilon$ . All terms in (3.48)–(3.51) are then of the same order,  $\epsilon^3$ . Symmetry breaking in the nonlinear terms would only appear at higher orders, as required for consistency.

Note also that we can eliminate some of the parameters in these equations by making suitable rescalings. Firstly, either  $\mu_r$  or  $\mu'_r$  may be scaled arbitrarily (by a positive factor), which means that only the *ratio*  $\mu'_r/\mu_r$  is important. Secondly, either  $a_r$  or  $b_r$  (but not both) could be scaled to  $\pm 1$  without loss of generality.

### 3.5.3 Results

We have looked for solutions to equations (3.48)–(3.51) in which the amplitudes remain constant (although the phases will vary with time). The results are shown in Table 3.5. Many of these branches were found analytically, with the remainder being computed numerically AUTO. Details of the derivations leading to Table 3.5 are given in Appendix C. The patterns are essentially the same as those found by Silber et al. (1992). The differences are that the solutions are slightly distorted in some cases by the presence

<i>Name of solution</i>	<i>Solutions for <math>(z_1, z_2, w_1, w_2)</math></i>	<i>Stability conditions</i>
rightward-travelling rolls (TRo <sup>R</sup> )*	$ z_1 ^2 = -\mu_r/a_r$ $d/dt(\arg z_1) = \mu_i + a_i z_1 ^2$ $z_2 = w_1 = w_2 = 0$	$a_r < 0$ $\mu'_r/\mu_r < b_r/a_r$
perpendicular travelling rectangles (TRe <sup>⊥</sup> )	$ z_1 ^2 = (\mu'_r b_r - \mu_r a_r)/(a_r^2 - b_r^2)$ $ w_2 ^2 = (\mu_r b_r - \mu'_r a_r)/(a_r^2 - b_r^2)$ $d/dt(\arg z_1) = \mu_i + a_i z_1 ^2 + b_i w_2 ^2$ $d/dt(\arg w_2) = \mu'_i + a_i w_2 ^2 + b_i z_1 ^2$ $z_2 = w_1 = 0$	$a_r < 0$ $ a_r  >  b_r $
rightward-travelling rectangles (TRe <sup>R</sup> )*	$ z_1 ^2 =  z_2 ^2 = \mu_r / -3a_r$ $d/dt(\arg z_1) = d/dt(\arg z_2) = \mu_i + 3a_i z_1 ^2$ $w_1 = w_2 = 0$	Always unstable
standing rolls (SRo)	$ z_1 ^2 = (\mu'_r b_r - \mu_r a_r)/(a_r^2 - b_r^2)$ $ w_1 ^2 = (\mu_r b_r - \mu'_r a_r)/(a_r^2 - b_r^2)$ $d/dt(\arg z_1) = \mu_i + a_i z_1 ^2 + b_i w_1 ^2$ $d/dt(\arg w_1) = \mu'_i + a_i w_1 ^2 + b_i z_1 ^2$	$a_r < 0$ $ a_r  >  b_r $ $ a  >  b $
standing rectangles (SRe)	$ z_1  =  z_2 ,  w_1  =  w_2 ,$ $\arg z_1 - \arg z_2 + \arg w_1 - \arg w_2 = 0$	
alternating rolls (ARo)	$ z_1  =  z_2 ,  w_1  =  w_2 ,$ $\arg z_1 - \arg z_2 + \arg w_1 - \arg w_2 = 0$	

\*There also exist leftward-travelling versions of these solutions (TRo<sup>L</sup> and TRe<sup>L</sup>), which may be obtained by exchanging  $z_1 \leftrightarrow z_2$ ,  $w_1 \leftrightarrow w_2$  and  $\mu \leftrightarrow \mu'$ .

**Table 3.5:** *The solutions found to equations (3.48)–(3.51), and their stability conditions (all of the listed conditions must be satisfied for the solution to be stable). Note that the SRe and ARo solutions were computed numerically with AUTO, hence the precise forms of the solutions and stability conditions are not listed in the table.*

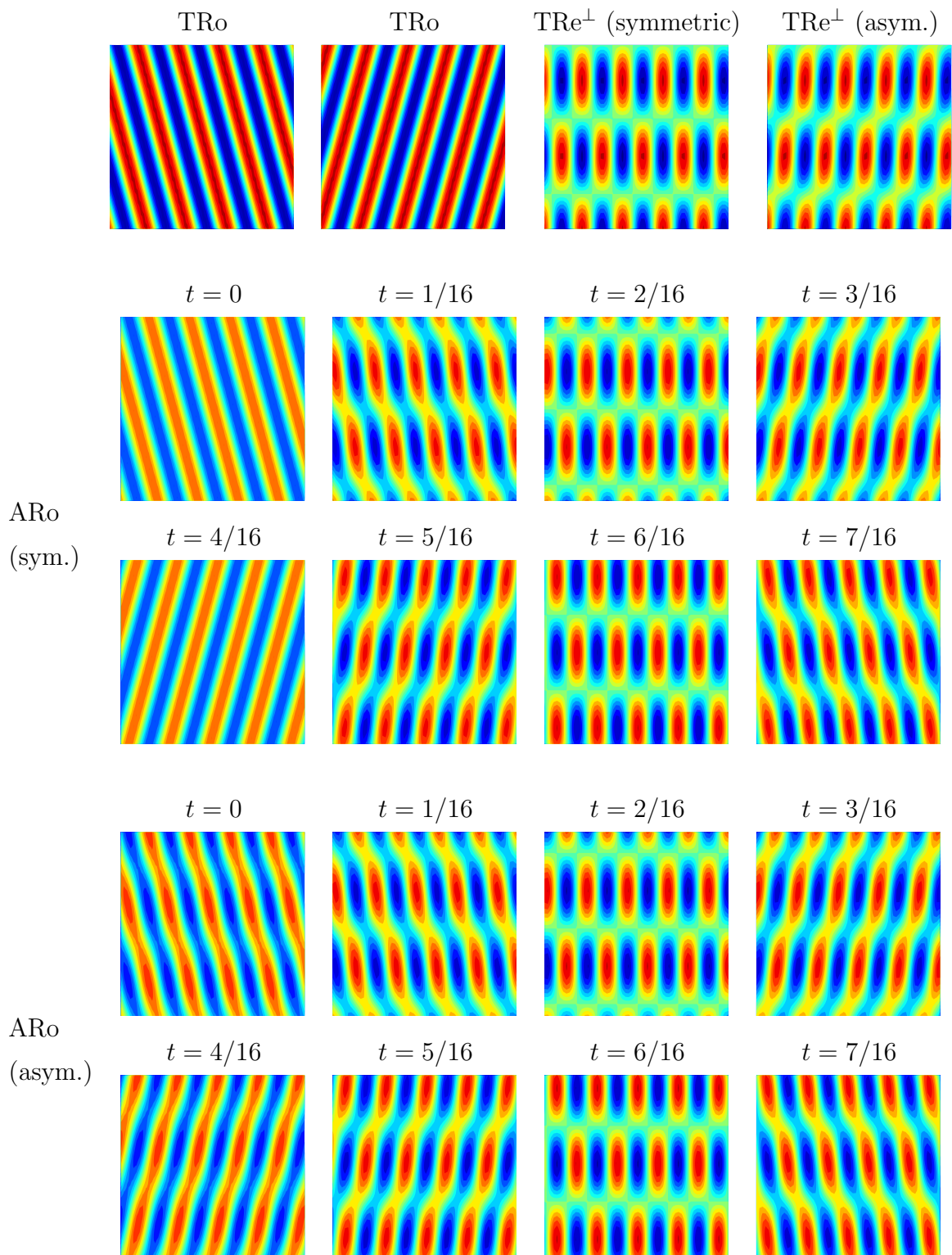
of asymmetry, and that there are sometimes two copies of each solution, one travelling left and one travelling right (whereas previously, these would have been related by symmetry). These separate left-going and right-going branches have been indicated by adding a superscript L or R where appropriate.

Figure 3.19 shows some of these patterns in graphical form. (We have taken the wavevectors  $\mathbf{k}_j$  to be at an angle of  $15^\circ$  to the  $x$ -axis in this picture.) The figure shows patterns both in the symmetric case (with all amplitudes equal) and in an asymmetric case (where the  $|w_j|$  have been taken to be 40% larger than the  $|z_j|$ ). The first row shows patterns which travel uniformly with time; TRo travel either left or right, while TRe $^\perp$  travel up or down (i.e. in the  $y$ -direction). The rest of the figure shows ARo, which have a more complicated time evolution. The ARo are essentially the same as the WR1 from the oscillatory hexagonal model (the only difference is that the angle between the constituent wavevectors is different).

Figure 3.20 shows our results for the existence and stability of the various solution branches in the different regions of the  $\mu_r$ - $\mu'_r$  plane. Note that only the *ratio*  $\mu'_r/\mu_r$  is important, so the regions are always sectors emanating from the origin, which have been represented by arcs on the diagrams. A solid (dashed) arc indicates the existence of a stable (unstable) solution. There are three cases (a)–(c) depending on  $a_r$  and  $b_r$ : case (a) applies when  $|b_r| < |a_r|$ , case (b) when  $|a_r| < |b_r| < 3|a_r|$ , and case (c) when  $|b_r| > 3|a_r|$ . In case (b), although the existence region of ARo can be calculated analytically, the stability region must be found numerically (it depends on all parameters including  $a_i$  and  $b_i$ ). In particular we cannot say explicitly whether the stability boundary will be inside or outside the sector AOB (this is represented by diagrams (b)(i) and (b)(ii)). Finally diagram (d) is not a separate case but rather shows some additional solution branches, which exist in all three cases, but are always unstable.

The diagram can be interpreted by observing that if  $\kappa$  is constant (the symmetric case) then we are on the forty-five degree line  $\mu_r = \mu'_r$ . Increasing the Rayleigh number corresponds to moving towards the top right. If we increase the variability of  $\kappa$  we move towards the top left, if  $\kappa$  decreases with depth, or the bottom right, if  $\kappa$  increases downward. (Recall that in our model,  $\kappa$  decreased downward so  $\mu'_r > \mu_r$  is the relevant part of the diagram.) For example in case (a) we would see TRe $^\perp$  and SRo for weakly varying  $\kappa$ , while for more strongly varying  $\kappa$  we would see only leftward-travelling rolls.

In addition to the solutions of Table 3.5, one or two other solution branches were found with AUTO. These had all four amplitudes ( $|z_1|$ ,  $|z_2|$ ,  $|w_1|$  and  $|w_2|$ ) unequal



**Figure 3.19:** Patterns in the rhombic model.

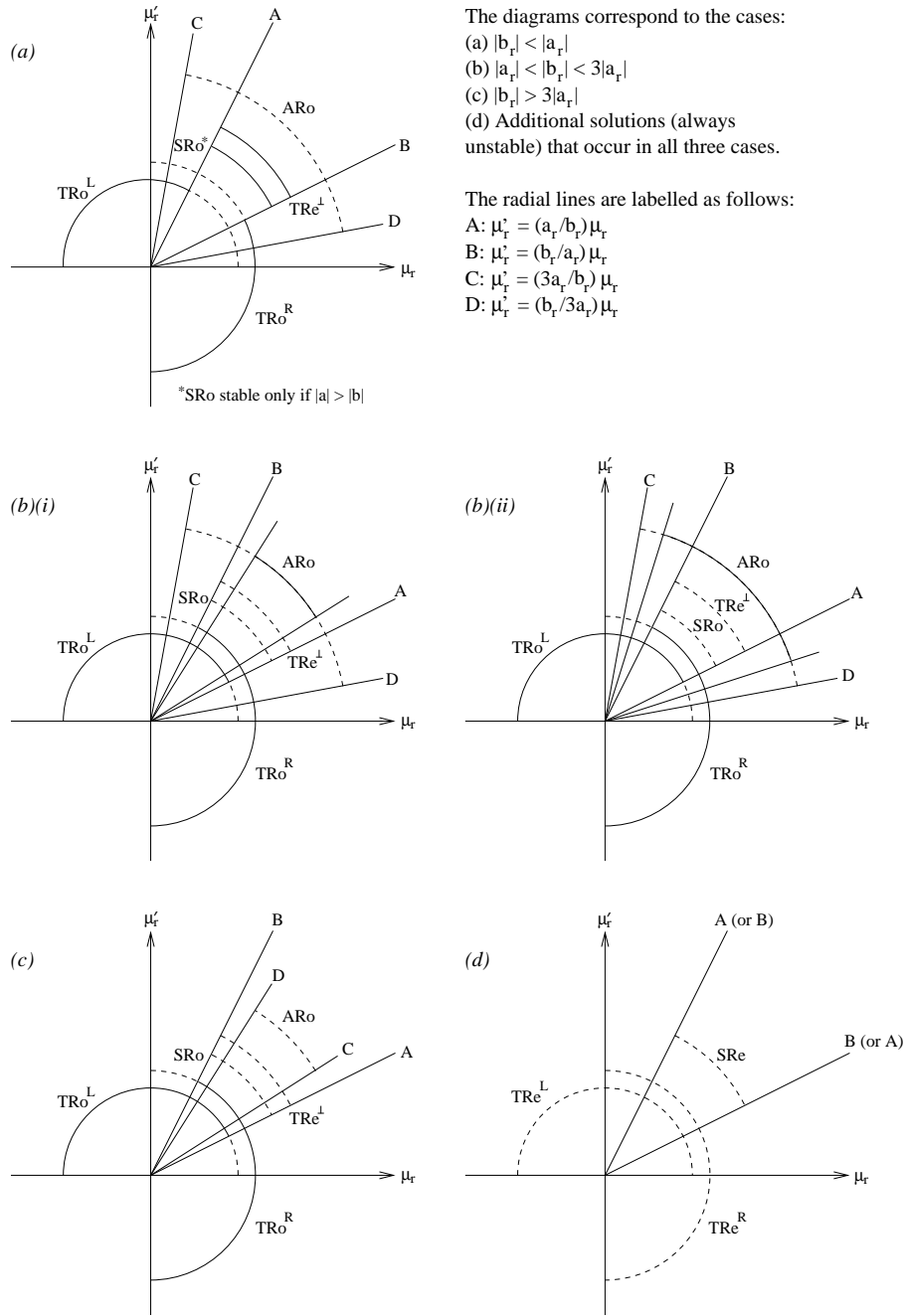


**Figure 3.20:** Regions of existence and stability of the various patterns in the  $\mu_r$ - $\mu'_r$  plane. Solid (dashed) curves indicate stable (unstable) solutions. See text for further explanation.

and non-zero. For example, solution branches of this kind were found that connected together the (unstable) standing rectangle branch and the travelling roll solutions. In some cases there were even solutions in which the amplitudes  $|z_j|$  and  $|w_j|$  were periodic functions of time. However, all of these more complicated solution branches were found to be unstable (at least for the cases we considered), so they are not discussed further here.

### 3.5.4 Comparison with results below the Lifshitz point

The results above apply to the oblique roll regime (above the Lifshitz point). However, the model (3.42)–(3.43) also applies below the Lifshitz point, i.e. when  $\phi < \phi_0$ , if we choose  $s_r > 0$  instead of  $s_r < 0$ . It is instructive to compare the results in the two different cases, since this illustrates how the solutions will change as  $\phi$  is increased through  $\phi_0$ , from the perpendicular into the oblique roll regime. (See also Figure 9 of Silber et al. 1992.)

In the ‘perpendicular’ regime ( $s_r > 0$ ) we have  $Q_c = P_c = 0$  (equation 3.44), so there are only two critical modes, representing left-going and right-going perpendicular rolls. We can obtain amplitude equations for these modes simply by setting  $z_1 = A$ ,  $w_1 = B$  in (3.42)–(3.43), and dropping all spatial derivative terms, which gives:

$$\dot{z}_1 = \mu z_1 + (a|z_1|^2 + b|w_1|^2)z_1 \quad (3.53)$$

$$\dot{w}_1 = \mu' w_1 + (a|w_1|^2 + b|z_1|^2)w_1 \quad (3.54)$$

(here we have also weakly broken the left-right symmetry). Note that these equations can alternatively be derived simply by setting  $z_2$  and  $w_2$  to zero in (3.48)–(3.51).

These equations have two solutions, corresponding to either travelling or standing rolls. In fact we can quite easily relate the existence and stability results for these solutions to the corresponding results in the oblique roll regime. We find that TRo exist and are stable below the Lifshitz point if and only if they exist and are stable above the Lifshitz point; in other words the stability conditions for TRo do not change between the perpendicular and oblique regimes. For the SRo, we find that the stability condition for SRo below the Lifshitz point corresponds to the stability condition for TRe<sup>⊥</sup> above the Lifshitz point; in other words, if TRe<sup>⊥</sup> are stable in the oblique regime then SRo will be stable in the perpendicular regime (and vice versa). This is all summarized in Figure 3.21 which shows the equivalent of Figure 3.20 for the perpendicular case.

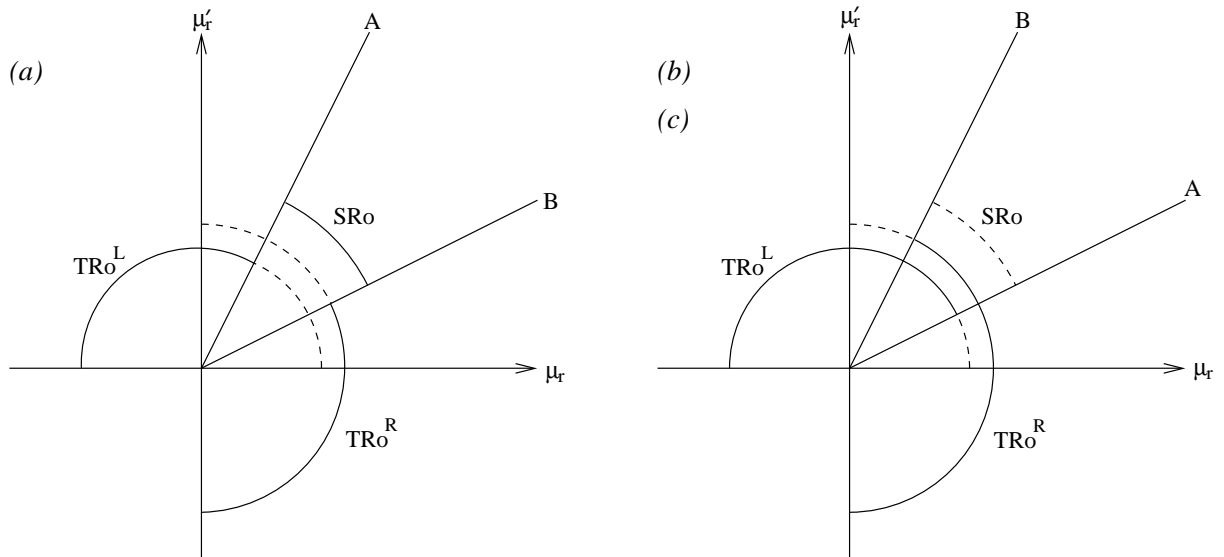


**Figure 3.21:** The equivalent of Figure 3.20, for the ‘perpendicular’ regime ( $\phi < \phi_0$ ,  $s_r > 0$ ) instead of the ‘oblique’ regime ( $\phi > \phi_0$ ,  $s_r < 0$ ). Note that in this case, there are only two possible solutions: perpendicular travelling rolls ( $TRo$ ) or perpendicular standing rolls ( $SRo$ ). The labels (a), (b), (c) and the lines A, B have the same meaning as in Figure 3.20.

We note therefore that one of the following would be observed if  $\phi$  was set to a value just below the Lifshitz point, and then increased to a value just above it:

- If the symmetry is very strongly broken, then only travelling rolls would be stable. These will be perpendicular rolls below the Lifshitz point, or oblique rolls above it.
- If the symmetry is not too strongly broken, and  $|b_r| > |a_r|$  (corresponding to cases (b) and (c) on Figures 3.20 and 3.21), then we will see again see travelling rolls on both sides of the Lifshitz point; we might also see alternating rolls above the Lifshitz point (depending on the values of  $\mu$ ,  $\mu'$ ,  $a$  and  $b$ ).
- If the symmetry is not too strongly broken, and  $|b_r| < |a_r|$  (corresponding to case (a) on Figures 3.20 and 3.21), then we will see perpendicular standing rolls below the Lifshitz point, and the  $TRe^\perp$  solution (see Figure 3.19) above it. If  $|a| > |b|$ , then we will also see oblique standing rolls above the Lifshitz point.

### 3.5.5 A calculation of the coefficients $a$ and $b$

In order to determine which of the above cases occur in any given problem, one needs to know the values of the coefficients  $a$  and  $b$ . These can be calculated by means of a perturbation analysis of the original equations about the equilibrium solution. In fact, we can calculate these coefficients for the symmetric case ( $\mu = \mu'$ ) if we want to, since their values do not change when the symmetry is weakly broken – the same values will apply to both the symmetric and asymmetric cases.

The symmetric case comes about when  $d\kappa/dz \rightarrow 0$ , i.e. when  $\kappa$  is uniform. Our assumptions also require us to choose  $\phi$  at (or just above) the Lifshitz point. It turns out that as  $d\kappa/dz \rightarrow 0$ , the value of  $\phi$  corresponding to the Lifshitz point tends to zero as well (see Figure 2.13 on page 61). In other words, if we let  $d\kappa/dz \rightarrow 0$  with  $\phi$  fixed just above the Lifshitz point, we will end up with  $\phi \rightarrow 0$  as well; therefore, it appears that the limit we require is that of a Boussinesq fluid (uniform  $\kappa$ ) in a vertical field.

Matthews and Rucklidge (1993) have performed a weakly nonlinear calculation in this limit. They actually use different magnetic boundary conditions to our model – they have the magnetic field constrained to be vertical at top and bottom (so  $B_x = B_y = 0$ ) while we have used a potential field at one boundary and a tied field at the other. Therefore the results will not apply directly to our model, but should still give a useful qualitative guide to what happens.

The calculation of Matthews and Rucklidge (1993) considered only the two-dimensional case. We can simulate this by setting  $z_2 = w_2 = 0$  (cf. equations 3.53–3.54), and also  $\mu = \mu'$ , obtaining the following equations, equivalent to theirs:

$$\dot{z}_1 = \mu z_1 + (a|z_1|^2 + b|w_1|^2)z_1 \quad (3.55)$$

$$\dot{w}_1 = \mu w_1 + (a|w_1|^2 + b|z_1|^2)w_1 \quad (3.56)$$

except that they now give explicit expressions for  $a$  and  $b$  ( $\gamma$  and  $\delta$  in their notation). Note that since, near the Lifshitz point, there are only two coefficients  $a$  and  $b$  to be determined ( $c$ ,  $d$  and  $f$  having been eliminated using equation 3.47), it is enough to consider only this two-dimensional problem.

These values can then be used to determine which of cases (a), (b) or (c) occurs as a function of the parameters  $Q$ ,  $\zeta$  and  $\sigma$  of the original PDEs. This has been done in Figure 3.22. Notice that case (c) does not in fact occur for this problem. The difference between (a)\* and (a) is that SRo are stable in the former ( $|a|$  being greater than  $|b|$  there) but unstable in the latter. The shaded region to the left of the diagram corresponds to

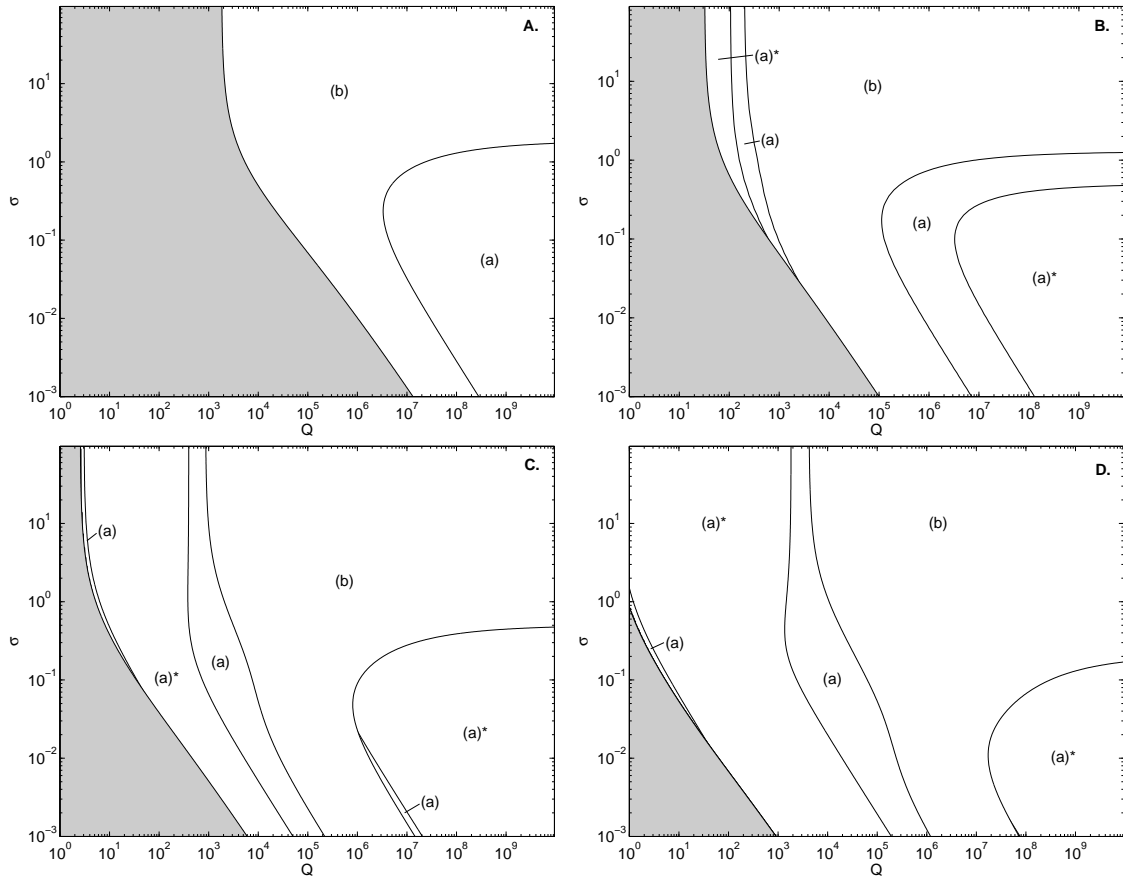


**Figure 3.22:** Diagrams showing which of the cases (a), (b) or (c) from Figure 3.20 occurs as a function of  $Q$ ,  $\zeta$  and  $\sigma$  (as indicated by the calculation of section 3.5.5). Note that in case (a), SRo may or may not be stable; the regions where SRo are stable have been marked with an asterisk. In the shaded areas, convection is steady at onset and the model does not apply. The four diagrams correspond to different values of  $\zeta$  as follows. A:  $\zeta = 0.9$ ; B:  $\zeta = 0.5$ ; C:  $\zeta = 0.1$ ; D:  $\zeta = 0.02$ .

parameter values in which convection is steady at onset (due to  $Q$  being too small) and hence the analysis does not apply here.

## 3.6 Conclusions

In this chapter, we have moved on from linearized computations and looked at some simplified nonlinear models. These can shed some light on what happens when the linear theory predicts several competing modes with similar growth rates. The great advantage of these models is that since they only use very general symmetry arguments, the results can be applied to a wide variety of situations. (For example, the results would in principle apply equally well to Boussinesq, anelastic, or compressible problems.) Their main disadvantage is that they apply only to the weakly nonlinear regime.

The method used was to select a lattice on which the solutions were to be doubly periodic. This restriction was essential for technical reasons, although it does limit the class of solutions that can be obtained. However, (approximately) doubly periodic patterns are frequently found experimentally or in numerical simulations, and therefore the method is useful in practice. Another limitation is that when we check for stability or instability of a pattern, we are in fact only checking for instability with respect to perturbations that are doubly periodic on the given lattice – for example, instabilities leading to long-wavelength modulations of the patterns will not be found by this method.

Our models were divided into two cases: the ‘steady’ case (for large  $\zeta$ ) and the ‘oscillatory’ case (for small  $\zeta$ ). We will describe each of these in turn.

The steady case is certainly the simpler of the two. Here, we investigated the problem on a hexagonal lattice (section 3.3). The hexagonal lattice is useful because it allows the competition between rolls and hexagons to be investigated; we would expect to see hexagonal patterns for small tilt angles  $\phi$  (because of the lack of up-down symmetry), but for larger tilt angles we would expect to see parallel rolls (Danielson, 1961). The steady hexagonal model allows this transition to be investigated in more detail.

The results show that when  $\phi = 0$ , the convection takes the form of steady hexagons (Figure 3.6, left-hand panel). As  $\phi$  increases, this pattern persists, although it becomes distorted in appearance (due to asymmetry between the three modes making up the hexagons; Figure 3.6, second and third panels). The hexagons also drift with a speed which is initially proportional to the tilt angle; the direction of travel was leftward in our model (see previous chapter), but this is model-dependent. When  $\phi$  is increased

further, there is a transition to steady parallel rolls; in many cases this transition is associated with hysteresis.

The oscillatory models showed slightly more complicated results. In this case we investigated two different models: one on a rhombic lattice (section 3.5), and one on a hexagonal lattice (section 3.4).

The oscillatory rhombic model included four modes, and was for simplicity restricted to values of  $\phi$  close to the Lifshitz point. If the amount of symmetry breaking was sufficiently weak, then there were essentially two cases. In the first case, standing rolls would be found below the Lifshitz point, while travelling rectangles (travelling in a direction perpendicular to the tilt), and possibly also standing rolls, would be found above it. In the second case, travelling rolls would be found below the Lifshitz point, while both travelling and (possibly) alternating rolls would be found above it.

The oscillatory hexagonal model was appropriate for small tilt angles, and had somewhat more complicated results (Figure 3.17). It is difficult to draw any conclusions relevant to sunspots from these results. We can however observe that there is a wide variety of interesting behaviour that can occur in this regime, even before considering fully nonlinear effects.

Note that in reality, the distinction between either a hexagonal or a rhombic lattice is somewhat artificial; modes from both lattices (plus an infinite number of other modes) would be present in the full problem. There is no real answer to this, but we can state that the hexagonal model is more appropriate to the perpendicular roll regime in the linear theory, occurring for small  $\phi$ , while the rhombic model is more appropriate to the vicinity of the Lifshitz point, which can be found at larger values of  $\phi$ . (Unfortunately, since we have to choose either one lattice or the other, we cannot really investigate the transition between these two regimes using these methods, except in the limited way that was discussed in section 3.5.4.)

We can now ask which of the two types of model – steady or oscillatory – is more relevant to sunspots. To answer this, we must consider the value of  $\zeta$  in the solar surface layers. In fact this value varies with depth due to ionization effects;  $\zeta < 1$  for depths less than 2000 km, but for depths of around 2000 to 20000 km there is a layer in which  $\zeta > 1$  (Meyer et al., 1974). Therefore, if the surface convective features observed in sunspots are fairly shallow (depth less than about 2000 km), the oscillatory model is appropriate. If their depth is much greater, then the steady model would be appropriate.

There is also another possibility: a combination of both the steady and the oscillatory

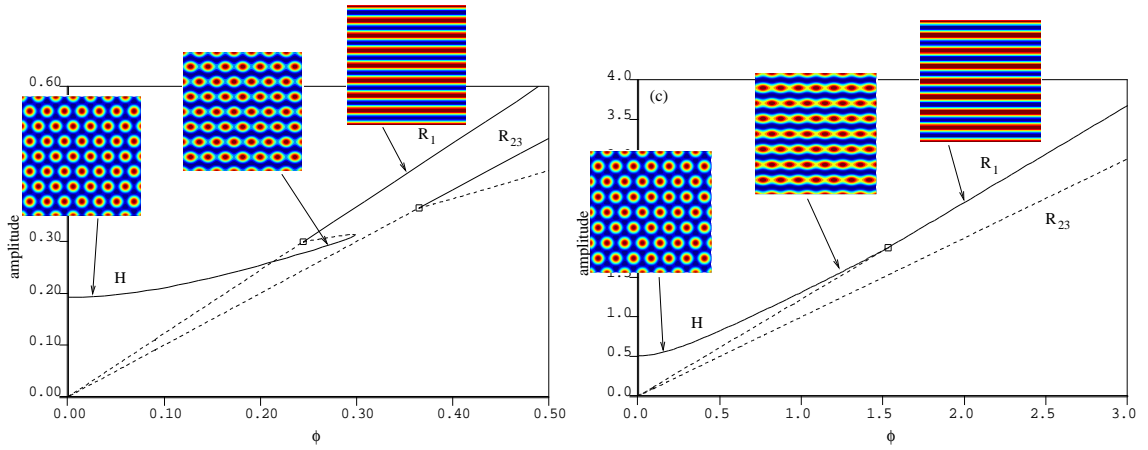


**Figure 3.23:** Bifurcation diagrams from the steady hexagonal model (with  $\theta = 30^\circ$ ), showing a case with hysteresis (left-hand picture) and one without (right-hand picture).

behaviour could occur simultaneously. In our models, we get either one or the other, because we consider only the situation near onset; for higher Rayleigh numbers, more complicated behaviour can occur. For example, the simulations of Weiss et al. (1990, 1996), in which  $\zeta$  is chosen to vary from 0.2 at the top of the layer to 2.2 at the base, show that convection is steady near onset, but as the Rayleigh number increases, a secondary bifurcation occurs, leading to a new solution. This solution consists of persistent overturning convection near the base of the layer, coupled to an oscillating pattern near the surface. (The models of this chapter cannot directly describe solutions of this kind; they would appear as secondary branches bifurcating from the solutions of our steady hexagonal model.)

Perhaps one of the most interesting features found in our models is the presence of hysteresis as  $\phi$  is varied. This is seen in both the steady and oscillatory cases (although we have only investigated the former in detail). Hysteresis is usually associated with sharp transitions between different patterns, and might therefore be part of the explanation for the sharp transition between the umbra and penumbra of a sunspot.

The hysteresis is illustrated in Figure 3.23 which shows bifurcation diagrams from the steady hexagonal model in two cases, one with and one without hysteresis. Pictorial representations of the stable solutions at various points have also been added.

Consider what would happen if  $\phi$  was allowed to vary smoothly with position, as a crude way of modelling a sunspot. In a case without hysteresis, the convection pattern would vary from regular hexagons in an area with a vertical field, to parallel rolls in

areas of large  $\phi$  (representing near-horizontal fields), with a smoothly varying pattern in between; this is illustrated by the right-hand diagram. By contrast, in a case with hysteresis, a rather more abrupt transition would be expected between the hexagon and roll regions (left-hand picture).

In the latter case, it is tempting to relate the hexagons to the umbra, and the rolls to the penumbra.<sup>2</sup> Of course, such a model would be highly simplified and idealized, and so could not be compared directly with observations. However, the mechanism that it represents is a very general one and we can reasonably expect it to apply to more complicated models as well (in addition to whatever else might be happening in those models).

The idea of hysteresis in magnetoconvection has also been employed by previous authors. For example, Rucklidge et al. (1995) suggest the presence of hysteresis as part of their explanation of the abrupt formation of penumbrae. Thomas and Weiss (2004) conjecture that hysteresis may be caused by the phenomenon of ‘flux pumping’. Our work suggests that hysteresis may also occur naturally as an intrinsic part of magnetoconvection in inclined fields.

We also note that a similar hysteresis phenomenon was found in the asymptotic calculation of Julien et al. (2000, 2003), although their model uses somewhat different assumptions to ours. (Both our model and theirs are highly idealized, albeit in different ways.) Moreover, they find a second hysteretic transition occurring for larger  $\phi$ , which they suggest is a possible explanation of the differing properties of bright and dark filaments. This second transition is not seen in our model, but since we assume small  $\phi$  we would not expect to see any effects associated with more strongly inclined fields.

In the next chapter we will describe how the steady hexagonal model of section 3.3 can be modified to include a tilt angle  $\phi$  that is a function of  $x$ . This will allow us to investigate the hysteresis phenomenon discussed above in more detail.

---

<sup>2</sup>The rolls do not capture the complex, filamentary structure found in real penumbrae, but we might suppose that such structure develops as a result of an instability starting from this roll state. However, such instabilities are beyond the scope of this weakly nonlinear theory.